Spin squeezing as a probe of many-body quantum correlations

Habilitationsschrift

Dr. Roman Schmied
Department of Physics
University of Basel, Switzerland

December 2016

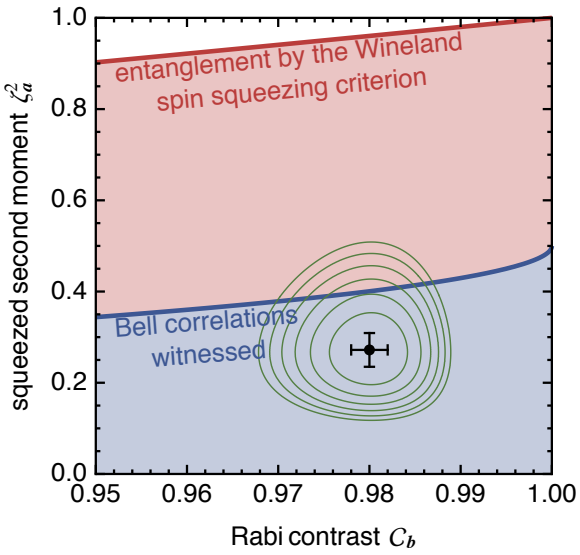

Whatever you say it is, it isn't.
—Alfred Korzybski

Contents

Outline

From 2010 to 2016 I have worked in the quantum atom optics lab, led by Prof. Philipp Treutlein, in the department of Physics at the University of Basel. During this time, my research has focused on the generation, detection, and use of entangled states of trapped atoms and ions. The present document gives an overview of this work, published in Refs. [1–12], which are attached at the end (starting on page 61).

In chapter 1 I discuss the topic of spin squeezing, both generally and specifically for Bose–Einstein condensates of rubidium-87 as observed in our lab. Details about the tomographic reconstruction of the generated quantum states are given, as well as a discussion of their use in metrology and their interest in fundamental quantum physics. This chapter represents the bulk of my work in Basel, and entitles this document. The quote given on the title page refers to this chapter: "Say whatever you choose *about* the object, and whatever you might *say* is not it." [13] I like to keep this advice in mind when thinking about our insights, to avoid confusing our empirical descriptions of measurements with the ontic, which remains as mysterious as ever.

Chapter 2 discusses lattice-based quantum simulators. It focuses on two topics: the design of optimized chip structures for generating two-dimensional arrays of microtraps to implement such quantum simulators, and a modified spin-wave theory that allows us to determine the approximate phase diagrams of such lattice models in order to focus our experimental efforts on the most interesting models and parameter ranges.

In chapter 3 I briefly present a one-semester course on Computational Quantum Mechanics that I have developed and taught repeatedly in Basel. This course is a pedagogic distillation of many practical skills and tools I have acquired during these years of scientific research.

Chapter 1

Spin squeezing in Bose–Einstein condensates

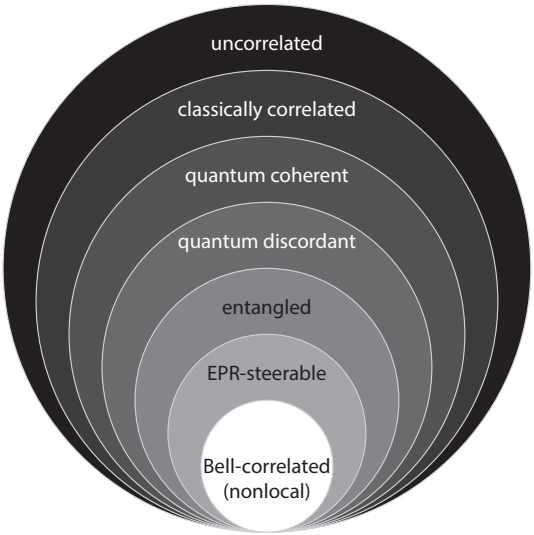

Figure 1.1: Schematic diagram of the Hilbert space of a set of quantum-mechanical particles. Correlations increase in strength from the outermost to the innermost circle. Entanglement, for example, is necessary but insufficient for Bell correlations. The various correlation strengths are close to each other at the bottom point, in the sense explained in section 1.6.

Hilbert space is vast. An ensemble of N qubits, with two internal states each, has a Hilbert space dimension of 2^N. There is no experiment that can ever hope to explore this space entirely, even for relatively small systems. The question of drawing a map of this enormous space thus appears naturally:

which states are at the same time *interesting* and *feasible*? By interesting I mean that the state either has a use in quantum metrology, quantum computing, quantum cryptography or a similar essentially-quantum field, or that it is of fundamental interest for discovering the workings of the quantum-mechanical world. There are many interesting but experimentally infeasible states, such as "Schrödinger cat" (GHZ) states for large N. On the other hand, there are many easily feasible but uninteresting states (from the quantum perspective), such as classical (coherent) states.

Spin-squeezed states are both feasible and interesting. They can be generated by a continuous transformation from a coherent spin state, for instance by one-axis or two-axis twisting [14], which makes them very robust, both to measurement noise and particle loss. Nonetheless, they manifest the strongest possible quantum-mechanical correlations even for small amounts of squeezing. Ideally, an infinitesimal amount of squeezing is sufficient to entangle the constituent atoms in a way that is of direct practical use in quantum metrology [7]. Going further, with a bit more than 3 dB of squeezing the atoms exhibit Bell correlations, which represent the most profound departure of quantum from classical physics. Thus it thus turns out that very interesting quantum-mechanical phenomena can be seen in states that are near classical states (see section 1.6 for a more quantitative statement). Figure 1.1 shows a very crude map of Hilbert space using different levels of correlations that can be detected between particles.

This chapter assembles the different pieces of work that have allowed us to gain more understanding in mapping the correlations between the particles of a many-body system.

1.1 Bose–Einstein condensation of rubidium-87

In our lab we experiment with two-component Bose–Einstein condensates (BECs) of rubidium-87 atoms. These bosonic alkali atoms have the convenient property that at low temperatures, the s-wave scattering lengths between particles in the different hyperfine states are all repulsive and of similar magnitude, which allows us to cool them by evaporation. Further, they can be laser-cooled at the easily available wavelength of 780 nm. Many properties of these atoms have been collected in Ref. [15]. Generating such a Bose–Einstein condensate is by now a well-known and well-described process. Briefly, a cloud of atoms is first trapped and cooled in a magneto-optical trap (MOT), transferred to a magnetic Ioffe–Pritchard (IP) trap, and from there into smaller and smaller IP traps while being cooled by radio-frequency (rf) evaporation. After Bose–Einstein condensation, an "rf knife" is used to reduce the number of particles in the BEC to the desired value.

In a BEC of atoms in a harmonic trapping potential, every atom occupies the same spatial wavefunction. This has two main advantages over using a

thermal cloud of atoms:

1. There is almost no residual entropy in a BEC. The BEC is surrounded by a very dilute cloud of thermal atoms, which carry all of the entropy of the ensemble; but as this thermal cloud is spatially separated from the much smaller BEC, it does not influence the BEC measurements done by absorption imaging. This entropy-free experimental starting point is advantageous for reductionistic studies: the influence of stimuli on the atomic system can be studied in the absence of noise coming from the initial state preparation. The BEC transition temperature $k_B T_c = 0.94\hbar\bar{\omega}N^{1/3}$ [16] is a factor of $N^{1/3}$ higher than the temperature needed for ground-state cooling, which makes reaching such a symmetric low-entropy state feasible in practice.

2. The collective BEC spatial wavefunction is symmetric under particle exchange. Since the total quantum state of an ensemble of bosons must always be symmetric under particle exchange, we thus conclude *a priori* that their internal (pseudo-spin) state must also be symmetric under particle exchange.[1] Although such a symmetric internal state can always be achieved by optically pumping all of the atoms into the same internal state (*i.e.* a symmetric product state), the BEC symmetry guarantees that thermal excitations do not subsequently reduce this symmetry.[2] This point will be important below, and is demonstrated experimentally in subsection 1.2.1.

Over the years, much work has been dedicated to improving the machine that generates and measures BECs in our lab. This machine, first built in Munich and subsequently transported to Basel, has seen impressive improvements in stability and precision. These improvements are part of the day-to-day work in a lab, and are not described in scientific publications; yet they are what periodically occupied most of my time. The hardware has been described in detail in the PhD theses of Philipp Treutlein [18], Pascal Böhi [19], Max Riedel [20], and Caspar Ockeloen [21]. The successive improvements can be tracked in our series of publications [1, 3, 7, 22, 23]. We are able to create Bose–Einstein condensates very reliably with anywhere from 50 to 3000 atoms, and study their thermodynamic properties with exquisite accuracy [3].

[1] The permutation symmetry of the total wavefunction is the product of the permutation symmetries of the external (spatial) wavefunction and the internal (spin or pseudo-spin) wavefunction. If both the total wavefunction and the external wavefunction are trivial representations of the symmetric permutation group, then the internal wavefunction must also be a trivial representation. See https://en.wikipedia.org/wiki/Representation_theory_of_the_symmetric_group.

[2] The symmetries of the spin state and the spatial state of the atoms can be lowered simultaneously by p-wave (and higher-wave) scattering. In ^{87}Rb clouds, these processes are negligible at temperatures below 100 μK [17]. Our BECs are typically at temperatures below 100 nK.

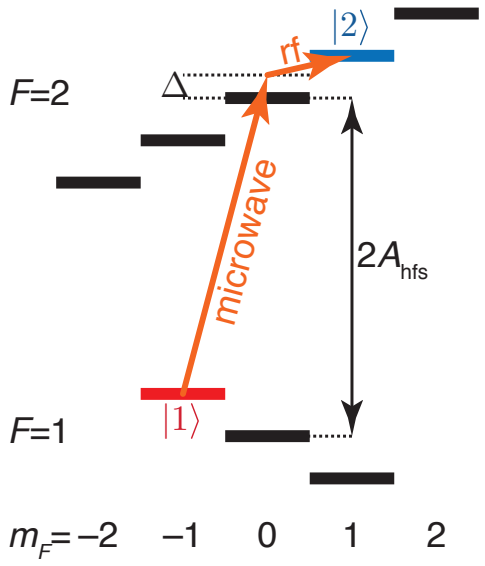

Figure 1.2: Schematic diagram of the hyperfine energy levels of a ^{87}Rb atom in the ground electronic state $5^2S_{1/2}$ in a weak magnetic field. Our experiments only populate the levels $|1\rangle = |F = 1, m_F = -1\rangle$ and $|2\rangle = |F = 2, m_F = 1\rangle$. We drive two-photon Rabi transitions between these two levels with a microwave-radiowave double resonance detuned by $\Delta \approx 500\,\mathrm{kHz}$ from the level $|F = 2, m_F = 0\rangle$.

Since the nuclear spin of ^{87}Rb is $I = 3/2$ and its electronic spin in the $5^2S_{1/2}$ ground state is $J = 1/2$, each atom has a total spin of either $F = 1$ or $F = 2$; these two sets of states are hyperfine-split by $2A_{\mathrm{hfs}} = 6.835\,\mathrm{GHz}$ [15] (see Figure 1.2). We single out the two hyperfine levels $|1\rangle \equiv |F = 1, m_F = -1\rangle$ and $|2\rangle \equiv |F = 2, m_F = 1\rangle$ for all experiments performed in our lab so far, because at the "magic" magnetic field of 3.23 G their differential Zeeman shift vanishes to first order, which makes these two levels particularly well suited for storing a qubit. Qubit lifetimes of many seconds, even minutes [24], have been observed in this system, albeit in more dilute clouds. These qubits can be manipulated simultaneously with resonant two-photon pulses consisting of a microwave (mw) field at around 6.835 GHz and a radio-frequency (rf) field chosen at around 1.8 MHz. By choosing the Rabi frequency of these manipulations ($\Omega \approx 500\,\mathrm{Hz}$) to be much slower than the detuning ($\Delta \approx 500\,\mathrm{kHz}$) to the intermediate state $|F = 2, m_F = 0\rangle$, we make sure that no hyperfine states other than $|1\rangle$ and $|2\rangle$ are ever measurably populated.

The internal state of each atom (indexed by $k = 1 \ldots N$) can thus be described by a pseudo-spin 1/2 (*i.e.* a qubit) with spin operator $\hat{\boldsymbol{s}}^{(k)} = \frac{1}{2}\hat{\boldsymbol{\sigma}}^{(k)}$ in terms of the Pauli vector $\hat{\boldsymbol{\sigma}} = \{\hat{\sigma}_x, \hat{\sigma}_y, \hat{\sigma}_z\}$. The total spin vector of the

entire ensemble,

$$\hat{\boldsymbol{S}} = \sum_{k=1}^{N} \hat{\boldsymbol{s}}^{(k)}, \tag{1.1}$$

also called the collective spin, is used to describe the properties of the atoms' internal states. As we have argued above, the total internal state is symmetric under particle exchange, which implies that the total spin vector of Equation (1.1) describes a spin of length $S = N/2$[3] (see subsection 1.2.1 for how to validate this experimentally). This means that we can describe the collective internal state of our BEC in the $(N+1)$-dimensional symmetric subspace of the 2^N-dimensional Hilbert space of N qubits. This dramatic simplification lies at the heart of the tomographic method and state visualization of section 1.7, but it is not necessary for our more fundamental conclusions of section 1.5 and section 1.6.

1.2 Spin measurements

Once we have created a Bose–Einstein condensate of N atoms in a particular quantum state of their internal degrees of freedom, we are interested in measuring various observables. The constraints on the available observables are:

1. The only measurement we can make is counting atoms in the different hyperfine states of the electronic ground state of ^{87}Rb. Specifically, for every produced BEC we destructively image the spatially resolved populations of the two states $|1\rangle$ and $|2\rangle$ after different times of flight, using resonant laser absorption. These images give us a moderate-resolution description of the momentum distribution of the atoms; however, in practice we do not rely on spatial information and integrate these atom numbers over the entire images in order to achieve atom counts with high signal-to-noise ratios. Effectively, our detection is equivalent to an almost number-resolved Stern–Gerlach experiment [25]. From the atom counts N_1 and N_2 in the two absorption images, we calculate the total atom number $N = N_1 + N_2$, the total spin $S = N/2 = (N_1 + N_2)/2$, and the spin projection quantum number $M = (N_1 - N_2)/2$.

2. Before determining the quantum state of the atoms, we can apply different unitary operations that act identically on each atom. Specifically, we can rotate the internal (qubit) state of each atom around the same spin axis by the same angle, by applying a combined mw/rf Rabi pulse. In this way, we can measure the spin projection quantum number M along any

[3] States with total spin $S = N/2 - 1, N/2 - 2, \ldots$ have lower symmetry and therefore cannot describe the collective internal state of an ideal BEC.

axis $\boldsymbol{d}$ and thus measure expectation values of observables depending on total-spin operators $\hat{S}_{\boldsymbol{d}} = \boldsymbol{d} \cdot \hat{\boldsymbol{S}}$.

Together, these constraints mean that for every measurement i we set the measurement axis orientation

$$\boldsymbol{d}_i = \boldsymbol{n}(\vartheta_i, \varphi_i) = \{\sin(\vartheta_i)\cos(\varphi_i), \sin(\vartheta_i)\sin(\varphi_i), \cos(\vartheta_i)\}, \tag{1.2}$$

and from the measured atom counts we determine the total spin S_i and the spin projection M_i along this axis. The tuples $(\vartheta_i, \varphi_i, S_i, M_i)$ are then used to extract various observables and quantifiers.

After much improvement, we are now able to measure atom numbers to within ± 4 atoms by absorption imaging [1]. We are also able to control the amplitudes and phases of internal spin states of the atoms with exquisite precision, allowing us to detect quantum fluctuations in the projection quantum numbers M_i with large signal-to-noise ratios. This means that we have succeeded in eliminating technical noise sources to such an extent that the remaining technical (classical) noise is much smaller than the quantum-mechanical noise, which cannot be eliminated. The variance of these quantum fluctuations is the quantity that we measure in order to detect correlations between the atoms in our BECs.

1.2.1 quantifying the total spin length

In order to validate the assumption that $S = N/2$, *i.e.* the assumption of operating in the symmetric subspace of N particles, we quantify the total spin length S by measuring $\langle \hat{S}_x^2 + \hat{S}_y^2 + \hat{S}_z^2 \rangle = S(S+1)$. This measurement is performed in two steps, using a coherent spin state. In a first experimental run, we prepare BECs in state $|1\rangle$ and measure their atom numbers $N_{1,z} \approx N$ and $N_{2,z} \approx 0$, from which we calculate $\langle \hat{S}_z^2 \rangle \approx N^2/4$. In a second experimental run, we rotate the internal state of each atom with a $\pi/2$ Rabi pulse into the coherent superposition $(|1\rangle + |2\rangle)/2$, and measure the atom numbers $N_{1,x} \approx N_{2,x} \approx N/2 \pm \sqrt{N}/2$, from which we calculate $\langle \hat{S}_x^2 \rangle \approx \langle \hat{S}_y^2 \rangle \approx N/4$. We do not need to perform separate measurements for the expectation values along the x- and y-axes, since these axes are only defined with respect to a phase that is indeterminate in the absence of a preferred phase frame. The ratio

$$\Upsilon = \sqrt{\frac{\langle \hat{S}_x^2 \rangle + \langle \hat{S}_y^2 \rangle + \langle \hat{S}_z^2 \rangle}{\frac{N}{2}(\frac{N}{2}+1)}} = \sqrt{2\left\langle \frac{(N_{1,x}-N_{2,x})^2}{(N_{1,x}+N_{2,x})(N_{1,x}+N_{2,x}+2)} \right\rangle + \left\langle \frac{(N_{1,z}-N_{2,z})^2}{(N_{1,z}+N_{2,z})(N_{1,z}+N_{2,z}+2)} \right\rangle} \tag{1.3}$$

estimates the quality of the approximation $S = N/2$, and therefore the accuracy of the assumption of a symmetric spin state. In our experiments, we

routinely achieve $\Upsilon > 97\%$. At present, we lack a model that describes the quantitative relationship between Υ and the quantum-mechanical state of the system; we operate under the assumption that a value of $\Upsilon \approx 1$ is sufficient to justify the approximation of a fully symmetric spin state.

1.3 Spin squeezing

In my opinion spin-squeezed states are the most practical quantum states to study mesoscopic quantum correlations. They are easy to generate by a continuous and slight transformation of a coherent spin state (see below), easy to characterize by their contrast and squeezed variance, and they cover the entire spectrum of quantum correlations of Figure 1.1 (see section 1.6). With two-component BECs (section 1.1) all of these operations have been demonstrated reliably in many laboratories.

Generating spin-squeezed states of Bose–Einstein condensates is by now a well-established technique in our lab, described in detail in the sequence of PhD theses of Pascal Böhi [19], Max Riedel [20], and Caspar Ockeloen [21]. Spin-squeezed states are generated from pure BECs by entangling the internal states of the constituent atoms.

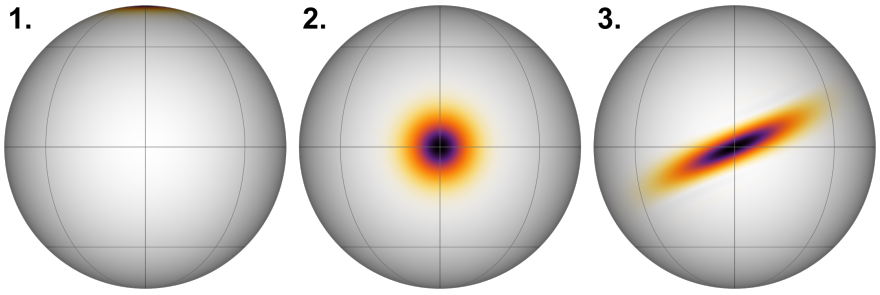

Figure 1.3: Three-step sequence for preparing a spin-squeezed state. The globes show the calculated Wigner distributions on the unit sphere [11] for $N = 40$ spins (*i.e.* total spin $S = 20$); color scale as in Figure 1.8. **1.** The spin-polarized coherent state $|S, S\rangle$ at the north pole (barely visible). **2.** The coherent spin state $|\frac{\pi}{2}, 0, S, S\rangle$ along the $+x$ axis. **3.** The spin-squeezed state $|\mu = 0.1\rangle$, Equation (1.4).

In the total-spin language of section 1.2, we generate spin-squeezed states by the following one-axis twisting scheme [14], shown graphically in Figure 1.3:

1. Start with a fully spin-polarized state where all atoms are in the $|1\rangle$ level. This state is the natural outcome of a clean BEC preparation process. It is a coherent spin state that can be described as the total-spin Dicke state $|S, S\rangle = |1\rangle^{\otimes N}$ in the $+z$ direction, where $N_1 = N$ and $N_2 = 0$.

2. Rotate by 90° around the $+y$ axis to generate the coherent spin state $|\frac{\pi}{2}, 0, S, S\rangle = \exp(-\mathrm{i}\frac{\pi}{2}\hat{S}_y)|S, S\rangle = \left[(|1\rangle + |2\rangle)/\sqrt{2}\right]^{\otimes N}$ pointing in the $+x$ direction. At this point, the internal states of the atoms are still unentangled. The required coherent rotation is achieved by a two-photon mw-rf double-resonance pulse that couples the two levels $|1\rangle$ and $|2\rangle$ (Figure 1.2); its absolute phase is irrelevant and rather defines what will become the $+y$ axis in the forthcoming manipulations.

3. Apply the one-axis-twisting Hamiltonian $\hat{H}_{\mathrm{oat}}(t) = \hbar\chi(t)\hat{S}_z^2$ during a time interval $[t_0, t_1]$ to find the squeezed state

$$|\mu\rangle = \exp\left(-\mathrm{i}\frac{\mu}{2}\hat{S}_z^2\right)|\frac{\pi}{2}, 0, S, S\rangle \tag{1.4}$$

with $\mu = 2\int_{t_0}^{t_1}\chi(t)\mathrm{d}t$ the total squeezing amplitude. In our system this nonlinear entangling Hamiltonian describes the evolution of a BEC in a potential that differs for the two internal states [22, 23]. Briefly, a spatially varying microwave near-field leads to microwave level shifts that depend both on the internal states and on the spatial positions of the atoms. Consequently, this state-selective and time-dependent force $\boldsymbol{F}(t)$ giving rise to the Hamiltonian $\hat{H}_{\mathrm{split}}(t) = -\boldsymbol{r}\cdot\boldsymbol{F}(t)|2\rangle\langle 2|$ spatially separates the atoms in state $|2\rangle$ from those in state $|1\rangle$; keep in mind, however, that every atom is in a coherent superposition of these two states. As a result of this spatial separation, inter-species collisions no longer take place, and the collisional phase shift accumulated during this separation depends on the square of the population difference between $|1\rangle$ and $|2\rangle$. More precisely, the instantaneous squeezing rate is [26]

$$\hbar\chi(t) = \frac{g_{11}}{2}\int|\psi_1(\boldsymbol{r})|^4\mathrm{d}^3\boldsymbol{r} + \frac{g_{22}}{2}\int|\psi_2(\boldsymbol{r})|^4\mathrm{d}^3\boldsymbol{r} - g_{12}\int|\psi_1(\boldsymbol{r})|^2|\psi_2(\boldsymbol{r})|^2\mathrm{d}^3\boldsymbol{r} \tag{1.5}$$

in terms of the instantaneous mode wavefunctions $\psi_i(\boldsymbol{r})$ (normalized to 1) and the coupling coefficients $g_{ij} = 4\pi\hbar^2 a_{ij}/m$ from the s-wave scattering lengths $\{a_{11}, a_{12}, a_{22}\} = \{100.40, 98.01, 95.44\}$ Bohr radii [27]. As long as the wavefunctions of the two states are approximately equal (*i.e.* overlapping), $\chi(t)$ is very small since the third term in Equation (1.5) cancels the first two; but when the state-selective force separates them spatially, the third term vanishes and $\chi(t)$ can reach values on the order of $1\,\mathrm{s}^{-1}$. During a typical experimental splitting sequence lasting a few tens of milliseconds, we thus reach values of μ on the order of $0.01\ldots0.1$.

The resulting state $|\mu\rangle$ still points along the $+x$ axis in the sense that $\langle\mu|\hat{S}_y|\mu\rangle = \langle\mu|\hat{S}_z|\mu\rangle = 0$, but it is spin-squeezed: along certain spin projection axes $\hat{S}_\zeta = \hat{S}_z\cos(\zeta) - \hat{S}_y\sin(\zeta)$, perpendicular to the $+x$ axis, its spin projection variance is less than that of a coherent spin state ($\mu = 0$). An analytic

calculation for the idealized situation [14] shows that

$$\langle\mu|\hat{S}_x|\mu\rangle = S\cos^{2S-1}\left(\frac{\mu}{2}\right) \tag{1.6a}$$

$$\langle\mu|\hat{S}_x^2|\mu\rangle = \frac{S(2S+1)}{4} + \frac{S(2S-1)}{4}\cos^{2S-2}(\mu) \tag{1.6b}$$

$$\langle\mu|\hat{S}_\zeta^2|\mu\rangle = \tfrac{S}{2} + S(2S-1)\sin(\zeta)\left\{\tfrac{\sin(\zeta)}{4}\left[1-\cos^{2S-2}(\mu)\right] - \cos(\zeta)\sin\left(\tfrac{\mu}{2}\right)\cos^{2S-2}\left(\tfrac{\mu}{2}\right)\right\}. \tag{1.6c}$$

For positive μ, the minimum of Equation (1.6)c is found at the squeezing angle

$$\zeta_{\mathrm{sq}} = \frac{1}{2}\tan^{-1}\left(\frac{4\sin\left(\frac{\mu}{2}\right)\cos^{2S-2}\left(\frac{\mu}{2}\right)}{1-\cos^{2S-2}(\mu)}\right). \tag{1.7}$$

The Wineland spin-squeezing parameter [28] is then defined as

$$\begin{aligned}\xi^2 &= \frac{2S\langle\mu|\hat{S}_{\zeta_{\mathrm{sq}}}^2|\mu\rangle}{\langle\mu|\hat{S}_x|\mu\rangle^2} \\ &= \frac{2S+3-(2S-1)\left\{\cos^{2S-2}(\mu)+\sqrt{\left[1-\cos^{2S-2}(\mu)\right]^2+\left[4\sin\left(\frac{\mu}{2}\right)\cos^{2S-2}\left(\frac{\mu}{2}\right)\right]^2}\right\}}{4\cos^{4S-2}\left(\frac{\mu}{2}\right)}.\end{aligned} \tag{1.8}$$

For small amounts of squeezing, this parameter ideally decreases from unity as $\xi^2 = 1-(S-1/2)\mu+\mathcal{O}(\mu^2)$. It serves as the quantity that characterizes the amount of metrologically usable spin-squeezing generated in an experiment: it measures the noise-to-signal ratio of an interferometric measurement, compared to that achieved with a coherent spin state (see section 1.4 and Ref. [7]). It is also an entanglement witness since separable states are guaranteed to yield $\xi^2 \geq 1$ (see section 1.5).

In the absence of experimental noise, the largest amount of squeezing (where ξ^2 is minimal) is achieved for a squeezing amplitude $\mu_* \approx S^{-2/3}$, where $\xi_*^2 \approx S^{-2/3}$ [14]; see Figure 1.5 for an example.

We further characterize the amount of squeezing by the distance between a spin-squeezed state $|\mu\rangle$ and an unsqueezed coherent spin state $|0\rangle = |\frac{\pi}{2}, 0, S, S\rangle$. For this we calculate the fidelity (overlap)

$$F(\mu) = |\langle\mu|0\rangle| \approx \left[1+\frac{S(2S-1)}{8}\mu^2\right]^{-1/4} \quad \text{for } |\mu| \lesssim \sqrt{\pi/S}. \tag{1.9}$$

At the squeezing maximum this fidelity is $F(\mu_*) \approx S^{-1/6}$. This means that for large systems (large S), maximally squeezed states are indeed far from coherent spin states, in the sense that they have a vanishing overlap. We can thus not claim to find maximal spin squeezing close to coherent spin states.

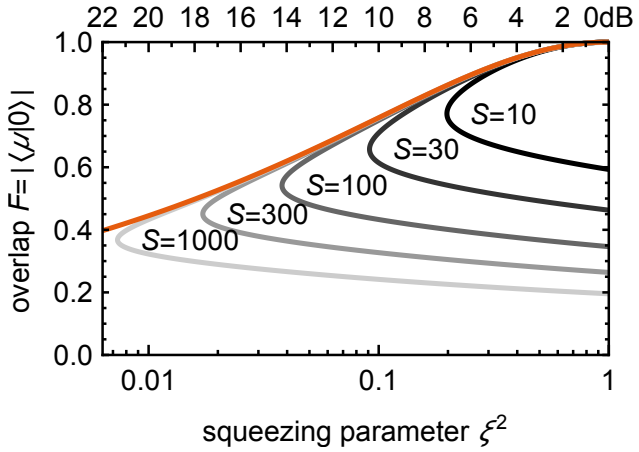

Figure 1.4: Overlap $F = |\langle\mu|0\rangle|$ with a coherent spin state as a function of the squeezing parameter $\xi^2(\mu)$, Equation (1.8), for ideal spin-squeezed states. The orange curve shows the asymptotic form for $S \to \infty$, Equation (1.10). The gray curves are numerically calculated values for finite S. The top axis shows the amount of squeezing in decibels, $-10\log_{10}(\xi^2)$.

The situation is different, however, in the experimentally more relevant case where we look at states with a fixed (given) squeezing parameter ξ^2, which are achieved with a squeezing amplitude of $\mu_{\xi^2} \approx (1-\xi^2)/(S\sqrt{\xi^2})$. For these states, the overlap with a coherent spin state is

$$F(\mu_{\xi^2}) \approx \sqrt{2\sqrt{\xi^2}/(1+\xi^2)} \qquad \text{for } S^{-2/3} \ll \xi^2 \leq 1, \tag{1.10}$$

independently of the system size S (*i.e.* independently of the number of particles in the system), as shown in Figure 1.4. What this means is that in order to achieve a given squeezing parameter ξ^2, we do not necessarily need to venture far from coherent spin states. In particular, spin-squeezed states with less than 10 dB of squeezing (*i.e.* $0.1 < \xi^2 < 1$) have an overlap with a coherent spin state of more than 75%; spin-squeezed states with less than 3 dB of squeezing (*i.e.* $0.5 < \xi^2 < 1$) have an overlap with a coherent spin state of more than 97%. In this sense, significant spin squeezing is found in the close vicinity of coherent spin states. In section 1.5 and section 1.6, we show that these spin-squeezed states, even though they are so close to classical (coherent) states, are nevertheless as profoundly quantum-mechanical as possible.

1.4 Quantum metrology

The most immediate application of spin-squeezed states is in quantum metrology, where the reduced variance of one spin component is used to make a measurement whose uncertainty will consequently be reduced. In Ref. [7] we have used spin-squeezed states of ^{87}Rb BECs to measure the amplitude of an oscillating magnetic field with a precision that surpasses the limits of what is possible without squeezing or entanglement. Due to the small physical size of the BEC, we can measure this amplitude at different positions in space by displacing the BEC between spin-squeezing and measuring.

Very generally, the lower limit on the achievable error variance of an observable $\hat{X}$ by a probe in quantum state $\hat{\rho}$ is given by the Cramér–Rao bound (CRB) [29]

$$(\Delta X)^2 = \mathrm{Tr}(\hat{\rho}\hat{X}^2) - \mathrm{Tr}^2(\hat{\rho}\hat{X}) \geq \frac{1}{\mathcal{F}(\hat{\rho}, \hat{X})}, \tag{1.11}$$

where $\mathcal{F}(\hat{\rho}, \hat{X})$ is the Fisher information. The more such information a state $\hat{\rho}$ contains (with respect to the observable $\hat{X}$), the more precise our measurement can potentially be. With respect to spin observables $\hat{X} = \hat{S}_{\boldsymbol{n}}$, coherent spin states have $\mathcal{F} = N$ (the standard quantum limit); the maximum possible value is $\mathcal{F} \leq N^2$ (the Heisenberg limit).

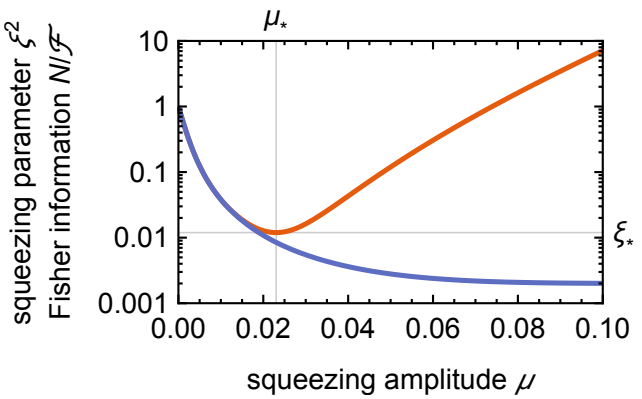

Figure 1.5: Spin-squeezing parameter ξ^2 [orange, Equation (1.8)] and reciprocal Fisher information $N/\mathcal{F}$ [blue, Equation (1.13)] calculated for $N = 2S = 1000$ particles in the absence of technical noise. The two quantities are indistinguishable for squeezing amplitudes $\mu \lesssim \mu_* = 0.023$. For larger μ, the states are over-squeezed but are still useful for quantum metrology if a suitable measurement protocol is employed.

In order to calculate the Fisher information of spin-squeezed states, we note that for any pure state $\hat{\rho} = |\psi\rangle\langle\psi|$ it is proportional to the variance of

the spin projection [29],

$$\mathcal{F}(\hat{\rho}, \hat{S}_{\boldsymbol{n}}) = 4\left[\langle\psi|\hat{S}_{\boldsymbol{n}}^2|\psi\rangle - \langle\psi|\hat{S}_{\boldsymbol{n}}|\psi\rangle^2\right]. \tag{1.12}$$

The maximum Fisher information of a spin-squeezed state is therefore found by aligning $\boldsymbol{n}$ with the anti-squeezed axis $\zeta = \zeta_{\text{sq}} + \frac{\pi}{2}$. The intuition for this picture is that a rotation of the spin-squeezed state around the anti-squeezed axis (*i.e.* a translation along the squeezed axis) is the fastest and most sensitive way to make the state orthogonal to itself (see Figure 1.3), which is essentially what the Fisher information measures [30]. For ideal spin-squeezed states we use Equation (1.6)c and Equation (1.7) to find

$$\begin{aligned}\mathcal{F}(\mu) &= 4\langle\mu|\hat{S}_{\zeta_{\text{sq}}+\frac{\pi}{2}}^2|\mu\rangle \\ &= \tfrac{S}{2}\left[2S+3-(2S-1)\left\{\cos^{2S-2}(\mu) - \sqrt{\left[1-\cos^{2S-2}(\mu)\right]^2 + \left[4\sin\left(\tfrac{\mu}{2}\right)\cos^{2S-2}\left(\tfrac{\mu}{2}\right)\right]^2}\right\}\right].\end{aligned} \tag{1.13}$$

We notice that $\mathcal{F}(\mu) = N/\xi^2 + \mathcal{O}(\mu^4)$: for small amounts of squeezing, the Fisher information is closely related to the spin-squeezing parameter (see Figure 1.5). More spin squeezing (smaller ξ^2) implies more Fisher information. In this way, the operational meaning of the spin-squeezing parameter as the improvement of an interferometric measurement's signal-to-noise ratio is mirrored by the theoretical description of measurement uncertainties through the CRB.

For larger amounts of squeezing, the two parameters decouple: the Fisher information keeps increasing while the squeezing parameter ξ^2 reaches a minimum and then increases dramatically. These so-called over-squeezed states (Figure 1.8) are no longer useful for quantum metrology directly based on extracting a measurement as a function of a spin projection $\langle\hat{S}_{\zeta_{\text{sq}}}\rangle$, since this measurement no longer has a reduced uncertainty. Instead, quantum-enhanced measurements that saturate the CRB must be extracted from higher moments $\langle\hat{S}_{\boldsymbol{d}}^k\rangle$ of spin projections ($k \geq 2$), which are increasingly difficult to measure experimentally as k increases. In the limit of maximum Fisher information $F(\pi) = N^2$ (the Heisenberg limit), contributions up to $k = 2S = N$ [similar to parity measurements $\langle(-1)^{\hat{S}_d}\rangle$] become necessary for quantum metrology to saturate the CRB. Such measurements are exceedingly difficult for large numbers of particles, and are completely destroyed by the loss of a single particle.

1.5 Quantum-mechanical entanglement

In Refs. [31–33] it is shown that spin squeezing in a BEC is an entanglement witness. Every separable state has $\xi^2 \geq 1$; measuring a spin-squeezing parameter of $\xi^2 < 1$ thus implies that the particles composing the system must be quantum-mechanically entangled.

In an ideal experiment, the squeezed regime $\xi^2 < 1$ is reached even for infinitesimally small squeezing amplitudes $\mu > 0$ [see Equation (1.8)]. Starting from a separable coherent spin state ($\mu = 0$), quantum-mechanical entanglement lies "just under the surface." In actual experiments, where technical noise both increases the numerator and decreases the denominator of Equation (1.8), we nonetheless easily reach the spin-squeezed regime of entangled particles [1, 7, 23], as shown exemplarily in Figure 1.6.

1.6 Bell correlations and quantum nonlocality

The strongest correlations allowed in our universe are Bell correlations (see Figure 1.1). These correlations are the resource that is necessary for violating a Bell inequality, and their existence demonstrates that the universe cannot be described with a locally causal model [34].

In Ref. [1] we have derived a simple criterion to determine whether Bell correlations are present in a many-particle quantum system. For this, we start with a recent Bell inequality [35] acting on a set of N qubits (*i.e.* particles) and find the condition

$$\frac{\langle \hat{S}_{\boldsymbol{a}}^2 \rangle}{N/4} \geq \frac{1}{2}\left[1 - \sqrt{1 - \left(\frac{\langle \hat{S}_{\boldsymbol{b}} \rangle}{N/2}\right)^2}\right] \tag{1.14}$$

for total-spin projections along two perpendicular measurement axes $\boldsymbol{a}$ and $\boldsymbol{b}$. This condition is satisfied for every state that is not Bell-correlated; violating it therefore demonstrates the presence of Bell correlations. Since the initial Bell inequality [35] depends only on symmetric one- and two-body correlation measurements, this condition depends only on first and second moments of the total spin operator $\hat{\boldsymbol{S}}$ introduced in section 1.2. And since only the scaled first and second moments appear in Inequality (1.14) (scaled in the sense that $\frac{\langle \hat{S}_{\boldsymbol{a}}^2 \rangle}{N/4} = \frac{\langle \hat{S}_{\boldsymbol{b}} \rangle}{N/2} = 1$ for a coherent spin state along the $\boldsymbol{b}$-axis), measurements for different total particle numbers N can be compared directly.

Figure 1.6 shows that we can violate Inequality (1.14) experimentally, and demonstrates that the internal states of the atoms in our BEC are Bell-correlated [1]. For an ideal spin-squeezed state and noiseless measurements, Inequality (1.14) can detect Bell correlations if $\mu \gtrsim \sqrt{2}/N + \mathcal{O}(N^{-3/2})$. Through Equation (1.9) this gives an overlap of about 97% with a coherent spin state at the onset of detectable Bell correlations for $N \to \infty$. Even though Bell correlations are stronger than entanglement (see Figure 1.1), and are in fact the strongest possible correlations allowed by quantum mechanics, they are found very close to a coherent spin state. It is not necessary to go to a completely different type of state or to go through a phase transition in order to create Bell correlations from a coherent spin state. This statement remains

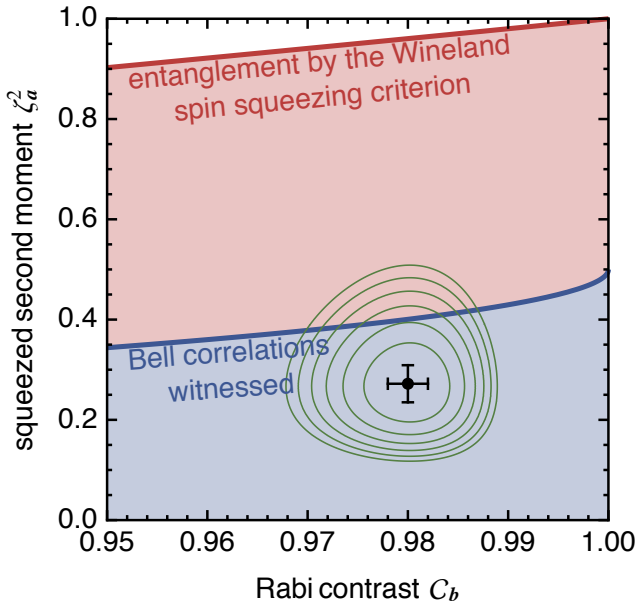

Figure 1.6: Observation of Bell correlations in a BEC. Black: our experimental data set of Ref. [1] expressed in terms of the Rabi contrast $\mathcal{C}_b = \frac{\langle \hat{S}_b \rangle}{N/2}$ and the squeezed second moment $\zeta_a^2 = \frac{\langle \hat{S}_a^2 \rangle}{N/4}$, with 1σ error bars. The green contours contain 90% (innermost), 99%, ..., 99.9999% (outermost) of the joint probability density for two random variables $\mathcal{C}_b$ (beta distribution on $[-1, 1]$) and ζ_a^2 (gamma distribution on $[0, \infty)$) matched to the data. Red shaded region: entanglement detected by spin-squeezing $\xi^2 < 1$ (section 1.5). Blue shaded region: Bell correlations detected by violation of our witness, Inequality (1.14).

true in the macroscopic limit: Bell correlations are not limited to microscopic systems where we would intuitively expect them. Like quantum-mechanical entanglement (section 1.5), Bell correlations lie just below the surface of classical (product) states.

Inequality (1.14) is not necessarily a tight witness: there may be many Bell-correlated states that satisfy it. In particular, we know that any pure entangled quantum many-body state is also Bell-correlated (the so-called Gisin theorem [36]), which means that some fraction of the entangled states between the red and blue curves in Figure 1.6 are likely to be Bell-correlated, even though we cannot yet detect this with the specific witness in Equation (1.14). A practical question is thus: among all possible Bell correlation witnesses, which one allows us to move the blue curve of Figure 1.6 to the largest possible values of ζ_a^2? We are planning to address this question in

future publications.

1.7 Quantum state tomography

In section 1.3, section 1.5, section 1.6, and Refs. [1, 5, 7] we use mean spins $\langle \hat{S}_{\boldsymbol{d}} \rangle$, mean squared spins $\langle \hat{S}_{\boldsymbol{d}}^2 \rangle$, and spin variances $\langle \hat{S}_{\boldsymbol{d}}^2 \rangle - \langle \hat{S}_{\boldsymbol{d}} \rangle^2$ to characterize the correlations between the atoms' internal states. Although these expectation values can be measured precisely, they only give a partial view of the quantum state of the BEC. In order to gain a fuller view, we have developed methods for quantum state tomography of the atoms' internal quantum state.

Quantum state tomography is the attempt to discover the quantum-mechanical state of a physical system [4, 11, 37]. The experimenter acquires a set of measurements of different non-commuting observables and tries to estimate what the density matrix of the systems must have been before the measurements were made, with the goal of being able to predict the statistics of future measurements generated by the same process. Once this density matrix is known, the expectation value of any observable can be deduced, even if no direct measurement scheme is known; and even unmeasurable quantities can be estimated, such as the purity $\mathrm{Tr}(\hat{\rho}^2)$, the entropy $-\mathrm{Tr}(\hat{\rho} \cdot \ln \hat{\rho})$, or the Fisher information (see section 1.4).

1.7.1 tomographic methods

In the context of the generation and characterization of non-classical states of Bose–Einstein condensates with internal degrees of freedom [11], the system under study is known to be in a totally symmetric state because of its Bose symmetry (see section 1.1). As described in Equation (1.1), these states are usually described in terms of total-spin observables, with the effective spin length equal to half the atom number (see subsection 1.2.1). In this restricted framework, quantum-state reconstruction is much more feasible than for general many-particle systems; for this reason, the reconstruction of spin (or pseudo-spin) density matrices is an important real-world case for quantum state tomography.

We have developed an algorithm to determine the density matrix of an N-particle system directly by measuring moments of total-spin projections along many projection axes [11]. This algorithm is simple and gives direct access to reduced density matrices: if we measure only up to the N'th moments of total-spin projections, we can still find the N'-particle reduced density matrix. The downside of this algorithm is that there is no guarantee that these (reduced) density matrices are positive semi-definite, which severely limits their usefulness, as described in detail in Ref. [4]. Further, the reduced N'-particle density matrices found with our method are not guaranteed to be the reductions of a full N-particle density matrix, which is a set of constraints that

is even stricter than positive semi-definiteness. For all of these reasons, the original backprojection algorithm of Ref. [11] has not been used much in our lab, but we have improved it as described in the following.

In Ref. [4] I have studied the problem of the tomographic quantum state reconstruction of a single qubit in great detail, which has clarified many issues related to large-system tomography, including questions on the preferred method, the treatment of measurement errors, and the proper interpretation of non-positive density matrices. As a result we have switched to using maximum-likelihood estimation (MLE) to determine tomographic density matrices. We use the $R\rho R$ algorithm [38], which is guaranteed to give positive semi-definite density matrices that maximize the likelihood of the observed data (assuming a Hilbert–Schmidt prior density on the space of density matrices). After we have adapted it to work with spin systems, this algorithm is feasible even for $N = 1000$ atoms using tens of thousands of spin projection measurement results (see Figure 1.8 for an example). N'-particle reduced density matrices can be computed from the resulting N-particle density matrix by partial tracing.

For these calculations, we first define the POVM[4] elements representing the state of the system into which it was projected by the ith measurement $(\vartheta_i, \varphi_i, S_i, M_i)$ for $i = 1 \ldots Q$ (see section 1.2). If all measurements were perfect, these POVM elements would be $\hat{\Pi}_i = |\vartheta_i, \varphi_i, S_i, M_i\rangle\langle\vartheta_i, \varphi_i, S_i, M_i|$ in terms of Dicke states along the projection axis of the ith measurement,

$$\begin{aligned} |\vartheta, \varphi, S, M\rangle &= e^{-\mathrm{i}\varphi\hat{S}_z} \cdot e^{-\mathrm{i}\vartheta\hat{S}_y} \cdot e^{-\mathrm{i}\varphi\hat{S}_z} \cdot |S, M\rangle \\ &= \sum_{\tilde{M}=-S}^{S} e^{-\mathrm{i}(M+\tilde{M})\varphi} d^S_{M,\tilde{M}}[\cos(\vartheta)]|S, \tilde{M}\rangle, \end{aligned} \quad (1.15)$$

where the $d^S_{M,\tilde{M}}(x)$ are Wigner d-matrix elements and $|S, M\rangle$ are Dicke states along the z-axis. If, however, each projective measurement has an estimated error $\delta M_i = \frac{1}{2}\sqrt{\sigma_1^2 + \sigma_2^2}$, with σ_k the estimated measurement errors on the detected atom numbers N_1 and N_2, then we define smoothed POVM elements

$$\hat{\Pi}_i = \frac{\sum_{M=-S_i}^{S_i} \exp\left[-\frac{(M-M_i)^2}{2\delta M_i^2}\right] |\vartheta_i, \varphi_i, S_i, M\rangle\langle\vartheta_i, \varphi_i, S_i, M|}{\sum_{M=-S_i}^{S_i} \exp\left[-\frac{(M-M_i)^2}{2\delta M_i^2}\right]}. \quad (1.16)$$

They represents our knowledge of the state of the system into which it was projected by the ith measurement. The tomographic reconstruction algorithm then starts with the unit matrix $\hat{\rho}_0 = \mathbb{1}/(2S+1)$, from which we iterate

$$\hat{R}_n = \sum_{i=1}^{Q} \frac{\hat{\Pi}_i}{\mathrm{Tr}(\hat{\rho}_n \cdot \hat{\Pi}_i)}, \qquad \hat{\rho}_{n+1} = \frac{\hat{R}_n \cdot \hat{\rho}_n \cdot \hat{R}_n}{\mathrm{Tr}(\hat{R}_n \cdot \hat{\rho}_n \cdot \hat{R}_n)}. \quad (1.17)$$

[4] Positive operator-valued measure: a measure on the space of positive semi-definite Hermitian operators.

This iteration has been shown to have the following properties:

- Each density matrix in the sequence $\hat{\rho}_0, \hat{\rho}_1, \hat{\rho}_2, \ldots$ is Hermitian and positive semi-definite.

- $\hat{\rho} = \lim_{n\to\infty} \hat{\rho}_n$ globally maximizes the likelihood of the measured data,

$$\mathcal{P}(\text{data}|\hat{\rho}) = \prod_{i=1}^{Q} \text{Tr}(\hat{\rho} \cdot \hat{\Pi}_i), \tag{1.18}$$

  over the space of positive semi-definite matrices, assuming that this space is fitted with a flat prior density.

We iterate this sequence until the trace distance $\frac{1}{2}\|\hat{\rho}_{n+1} - \hat{\rho}_n\|_1$ becomes sufficiently small, usually on the order of 10^{-8} or less. For this purpose I have written an efficient and portable computer program in the C programming language. The input of this program consists of a text file describing each projective measurement by a tuple $(\vartheta_i, \varphi_i, S_i, M_i, \delta M_i)$ for $i = 1 \ldots Q$: the ith projective measurement along the quantization axis $\boldsymbol{d}_i = \{\sin(\vartheta_i)\cos(\varphi_i), \sin(\vartheta_i)\sin(\varphi_i), \cos(\vartheta_i)\}$ has detected a total of $N_i = 2S_i = N_1^{(i)} + N_2^{(i)}$ atoms and a projection quantum number $M_i = (N_1^{(i)} - N_2^{(i)})/2$; the estimated error on M_i is δM_i. In order to generate a density matrix of size $(2S+1) \times (2S+1)$, the input of my MLE code needs the total spin S (total atom number N) of each measurement to be the same. Since the total atom number in every experimental BEC is different, we must scale the raw data by first calculating the mean atom number $\bar{N}$ of all measurements, and then scaling every measured projection quantum number to $M_i = M_{i,\text{raw}} \times \bar{N}/N_i$. Since in practice the fluctuations of N are relatively small, on the order of $\sqrt{N}$ or less, this distortion is considered acceptable. If the total particle number fluctuates more strongly, post-selecting a narrow range of particle numbers before tomographic inversion may be required.

The output of my MLE code is a file containing $2(2S+1)^2$ 64-bit floating-point numbers representing the real and imaginary parts of the coefficients of the reconstructed density matrix in the basis of Dicke states.

The main difficulty in writing this MLE code was to find a stable and fast algorithm to calculate Wigner d-matrices for large angular momenta, in order to evaluate the coefficients of the states of Equation (1.15). To calculate these matrix elements $d^S_{M,\tilde{M}}(x)$ with $x = \cos(\vartheta)$, we first use the symmetries $d^S_{M,\tilde{M}}(x) = (-1)^{\tilde{M}-M} d^S_{-M,-\tilde{M}}(x) = (-1)^{\tilde{M}-M} d^S_{\tilde{M},M}(x) = (-1)^{S-M} d^S_{M,-\tilde{M}}(-x)$ to reduce the calculation to the cases where $M \geq 0$, $|\tilde{M}| \leq M$, $0 \leq x < 1$

[with the limiting case $d^S_{M,\tilde{M}}(1) = \delta_{M,\tilde{M}}$]. Then we use the stable recursion

$$d^S_{S,\tilde{M}}(x) = \sqrt{\binom{2S}{S-\tilde{M}}} \left(\frac{1-x}{2}\right)^{\frac{S-\tilde{M}}{2}} \left(\frac{1+x}{2}\right)^{\frac{S+\tilde{M}}{2}}, \tag{1.19a}$$

$$d^S_{S-1,\tilde{M}}(x) = (Sx - \tilde{M}) d^S_{S,\tilde{M}}(x) \sqrt{\frac{2}{S(1-x^2)}}, \tag{1.19b}$$

$$d^S_{M,\tilde{M}}(x) = \frac{(2S-1)[S(S-1)x - M\tilde{M}] d^{S-1}_{M,\tilde{M}}(x) - S\sqrt{[(S-1)^2 - M^2][(S-1)^2 - \tilde{M}^2]}\, d^{S-2}_{M,\tilde{M}}(x)}{(S-1)\sqrt{(S^2-M^2)(S^2-\tilde{M}^2)}}. \tag{1.19c}$$

1.7.2 graphical representation: Wigner distribution

The state of a quantum-mechanical spin-S system is given abstractly by its density operator $\hat{\rho}$, which we can determine tomographically as in the previous section. This operator is most commonly represented by the density matrix with elements $\rho_{M,M'} = \langle S, M|\hat{\rho}|S, M'\rangle$ expressed in the Dicke basis with $M, M' \in \{-S, -S+1, -S+2, \ldots, +S\}$. This density matrix facilitates calculations but does not lend itself to direct qualitative interpretation.

The Wigner quasi-probability distribution [39] $W(\Theta, \Phi)$ is an alternative representation of a quantum spin state. It is a real-valued function on the unit sphere with the following properties:

1. It is linear in the density operator $\hat{\rho}$.

2. It is normalized as $\int_0^{\pi} \sin(\Theta) d\Theta \int_0^{2\pi} d\Phi\, W(\Theta, \Phi) = \sqrt{\frac{4\pi}{2S+1}}\, \mathrm{Tr}(\hat{\rho}) = \sqrt{\frac{4\pi}{2S+1}}$.

3. The Wigner distribution associated with a coherent spin state is approximately a Gaussian centered at the direction of the state (see below). The coherent spin state $|S, M = S\rangle$ is centered at the north pole; that of $|S, M = -S\rangle$ is centered at the south pole. The coherent spin state $|\vartheta, \varphi, S, S\rangle$ defined in Equation (1.15) is centered at $\boldsymbol{n}(\vartheta, \varphi) = \{\sin(\vartheta)\cos(\varphi), \sin(\vartheta)\sin(\varphi), \cos(\vartheta)\}$.

4. The operators $\hat{S}_x$, $\hat{S}_y$, $\hat{S}_z$ are the generators of state rotations around their respective Cartesian axes; their effects on the Wigner distribution are corresponding rotations of the unit sphere. For example, for a rotation by an angle α around the z-axis, we have the equivalence

$$\hat{\rho}_\alpha = e^{-i\alpha\hat{S}_z} \cdot \hat{\rho} \cdot e^{i\alpha\hat{S}_z} \quad \leftrightarrow \quad W_\alpha(\Theta, \Phi) = W(\Theta, \Phi - \alpha) \tag{1.20}$$

Rotations around other axes have equivalent geometric interpretations.

These properties allow us to interpret the Wigner distribution geometrically and to use it to plan and analyze experiments.

We define the Wigner quasi-probability distribution on the unit sphere as a sum over spherical harmonics [11, 40, 41],

$$W(\Theta, \Phi) = \sum_{k=0}^{2S} \sum_{q=-k}^{k} \rho_{kq} Y_k^q(\Theta, \Phi), \tag{1.21}$$

with $\rho_{k,-q} = (-1)^q \rho_{k,q}^*$ so that $W(\Theta, \Phi) \in \mathbb{R}$. The coefficients of this expansion are calculated from the density matrix elements with

$$\rho_{kq} = \sum_{M=-S}^{S} \sum_{M'=-S}^{S} t_{kq}^{SMM'} \langle S, M|\hat{\rho}|S, M'\rangle, \tag{1.22}$$

where we have defined the modified Clebsch–Gordan coefficients [11]

$$t_{kq}^{SMM'} = (-1)^{S-M'} \langle S, M; S, -M'|k, q\rangle. \tag{1.23}$$

These latter coefficients satisfy the orthogonality relations

$$\sum_{M=-S}^{S} \sum_{M'=-S}^{S} t_{kq}^{SMM'} t_{k'q'}^{SMM'} = \delta_{kk'}\delta_{qq'}, \tag{1.24a}$$

$$\sum_{k=0}^{2S} \sum_{q=-k}^{k} t_{kq}^{SMM'} t_{kq}^{SM''M'''} = \delta_{MM''}\delta_{M'M'''}. \tag{1.24b}$$

This means that the transformation of Equation (1.22) is unitary and is the spherical equivalent of a Fourier transform; it satisfies an equivalent of Parseval's theorem,

$$\sum_{k=0}^{2S} \sum_{q=-k}^{k} |\rho_{kq}|^2 = \|\hat{\rho}\|_{\mathrm{F}}^2 = \mathrm{Tr}(\hat{\rho}^2), \tag{1.25}$$

where $\|\cdot\|_{\mathrm{F}}$ is the Frobenius norm. Therefore, conversions between the Wigner distribution and the density operator can be done without loss of information. A graphical representation of the Wigner distribution is thus a valid and detailed way of representing a density operator. Further, as opposed to the coefficients of the density matrix $\langle S, M|\hat{\rho}|S, M'\rangle$, the coefficients of the Wigner distribution ρ_{kq} are naturally ordered into broad structures (small k) and fine structures (large k).

coherent spin states

From the list of properties given above, we conclude that the Wigner distribution of the density operator $|\vartheta, \varphi, S, S\rangle\langle\vartheta, \varphi, S, S|$ of a coherent spin state

[see Equation (1.15)] depends only on the angle between the direction $\boldsymbol{n}(\vartheta, \varphi)$ of the coherent spin state and the direction $\boldsymbol{n}(\Theta, \Phi)$ in which we are evaluating the Wigner distribution,

$$W_{\vartheta,\varphi}(\Theta, \Phi) = \sqrt{\frac{4\pi}{2S+1}} \times \omega_S[\boldsymbol{n}(\Theta, \Phi) \cdot \boldsymbol{n}(\vartheta, \varphi)]. \tag{1.26}$$

Its angular dependence is given by the normalized "spherical Gaussian" functions

$$\begin{aligned}\omega_S(x) = \sum_{k=0}^{2S} \frac{2k+1}{4\pi} \sqrt{\frac{(2S)!(2S+1)!}{(2S-k)!(2S+k+1)!}} P_k(x) \\ \approx \frac{2S+3/2}{2\pi} e^{-(2S+3/2)(1-x)},\end{aligned} \tag{1.27}$$

defined in terms of Legendre polynomials; the approximation is valid for $S \gg 1$. These functions are normalized Gaussians in the sense that $\omega_S(\cos\vartheta)$ is close to a Gaussian centered at the north pole, with normalization $2\pi \int_{-1}^{1} \omega_S(x)\mathrm{d}x = 1$ and angular size

$$\langle [2\sin(\vartheta/2)]^2 \rangle = 2\pi \int_{-1}^{1} 2(1-x)\omega_S(x)\mathrm{d}x = 2\left(1 - \sqrt{\frac{S}{S+1}}\right) \approx (S+3/4)^{-1}. \tag{1.28}$$

They are not strictly positive, but instead their tails oscillate around zero with a negligible amplitude on the order of 2^{-2S}.

Gaussian smoothing on the unit sphere

We define a quasi-Gaussian smoothing operation on the unit sphere as the convolution of any spherical function $f(\Theta, \Phi)$ with a smoothing kernel $\omega_g(x)$ from Equation (1.27),

$$\begin{aligned}f_g(\Theta, \Phi) = (f * \omega_g)(\Theta, \Phi) = \int_0^{\pi} \sin\vartheta \mathrm{d}\vartheta \int_0^{2\pi} \mathrm{d}\varphi f(\vartheta, \varphi) \\ \times \omega_g[\cos(\Theta)\cos(\vartheta) + \sin(\Theta)\sin(\vartheta)\cos(\Phi - \varphi)].\end{aligned} \tag{1.29}$$

We note that although g here has the appearance of an angular momentum (with $2g \in \mathbb{N}_0$), it need not correspond to any physical quantity and is merely used to parameterize the width of the smoothing kernel in a particular application [see Equation (1.28)]. In the special case of smoothing a spherical harmonic with such a Gaussian kernel we find [40]

$$(Y_k^q * \omega_g)(\Theta, \Phi) = \begin{cases} \sqrt{\frac{(2g)!(2g+1)!}{(2g-k)!(2g+k+1)!}} \times Y_k^q(\Theta, \Phi) & \text{if } 0 \le k \le 2g, \\ 0 & \text{if } k > 2g. \end{cases} \tag{1.30}$$

The form of these damping prefactors $\sqrt{\frac{(2g)!(2g+1)!}{(2g-k)!(2g+k+1)!}} \approx \exp\left[-\frac{k(k+1)}{2(2g+1)}\right]$ confirms the intuition that a quasi-Gaussian smoothing operation damps small-wavelength (large k) structures faster than long-wavelength (small k) structures.

By convolving or anti-convolving the Wigner distribution, Equation (1.21) with a spherical Gaussian kernel, Equation (1.30),

$$W_g(\Theta,\Phi) = \sum_{k=0}^{2S}\sum_{q=-k}^{k} \rho_{kq}\left[\frac{(2g)!(2g+1)!}{(2g-k)!(2g+k+1)!}\right]^{\frac{1}{2}} Y_k^q(\Theta,\Phi), \quad (1.31)\text{a}$$

$$W_{-g}(\Theta,\Phi) = \sum_{k=0}^{2S}\sum_{q=-k}^{k} \rho_{kq}\left[\frac{(2g)!(2g+1)!}{(2g-k)!(2g+k+1)!}\right]^{-\frac{1}{2}} Y_k^q(\Theta,\Phi), \quad (1.31)\text{b}$$

we calculate Agarwal's generalized phase-space distributions [40]. Specifically:

$g = \pm\infty$: The Wigner distribution itself, $W(\Theta,\Phi) = W_{\pm\infty}(\Theta,\Phi)$, is the only generalized phase-space distribution that satisfies Parseval's theorem, Equation (1.25), and is therefore on an equal footing with the density operator $\hat{\rho}$.

$g = -S$: The Glauber–Sudarshan P representation $P(\Theta,\Phi) = W_{-S}(\Theta,\Phi)$ is found by anti-convolving the Wigner distribution of the state with that of a coherent state of equal angular momentum S, Equation (1.26). The P representation contains exaggerated fine structure since large-k components are strongly amplified in this anti-smoothing operation. It is useful as a way to calculate reduced density matrices of symmetric states (section 1.2): the P representation of the N'-particle reduced density matrix is found from the P representation of the full $N = 2S$-particle density matrix by setting all coefficients with $k > N'$ to zero [42].

$g = S$: The Husimi–Kano Q representation $Q(\Theta,\Phi) = W_S(\Theta,\Phi)$ is found by convolving the Wigner distribution of the state with that of a coherent state of equal angular momentum S, Equation (1.26). The Q representation contains less information than the Wigner distribution, since high-frequency (large-k) contributions are strongly damped in this convolution. In particular, this smoothing operation averages out all negative regions of the Wigner function, such that $Q(\Theta,\Phi) \geq 0$.

$g \gg S$: Smoothing operations with $g \gg S$ can be used to include measurement uncertainties into tomographic results, see subsection 1.7.3 and Figure 1.8.

1.7.3 interpretation of tomographic results

The top panel of Figure 1.8 shows an example of a tomographically determined quantum state of a one-axis-twisted (over-squeezed) Bose–Einstein conden-

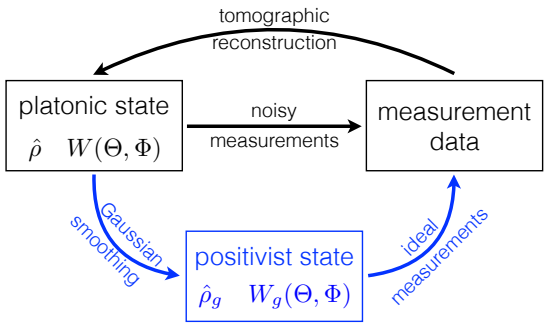

Figure 1.7: Schematic of tomographic quantum states. The platonic state $\hat{\rho}$ and its associated Wigner distribution $W(\Theta,\Phi)$ are the results of a tomographic process as described in subsection 1.7.1, using the noisy measurement operators of Equation (1.16). The statistics of further measurement data are predicted using the same noisy measurement operators (black arrow). By splitting this noisy measurement process into its two components, (i) the addition of noise though a smoothing operation, and (ii) the noise-free projective measurement (blue arrows), the positivist quantum state $W_g(\Theta,\Phi)$ is introduced as a representation of our actual knowledge of the system including the measurement inaccuracies.

sate (see section 1.3). We see immediately that this state has much small-scale structure that probably does not represent real experimental features. The reason for this extra structure is that, in the nomenclature of section 3.1 of Ref. [4], the reconstructed density matrix is a *platonic* quantum state. It represents our knowledge of the state prior to measurement, *i.e.* without including noise introduced by our measurement operators, Equation (1.16) (see Figure 1.7). Our measurement uncertainties δM_i smooth this exaggerated small-scale structure through Equation (1.16) upon measurement, so that no such fine structure could ever be detected with the present setup. For this reason, Ref. [4] recommends constructing a *positivist* quantum state that already includes the measurement uncertainty, and that therefore does not exhibit exaggerated (unmeasurable) small-scale structure. As shown in the blue part of Figure 1.7 this positivist state re-defines the quantum system to include the measurement inaccuracies, instead of artificially separating the quantum system from the measurement procedure.

In order to construct the positivist quantum state, we convolve the platonic (reconstructed) Wigner distribution with the Wigner distribution of a coherent spin state of angular momentum g (subsection 1.7.2). The effective angular momentum of this convolution, which is $g = 524$ in the present case, is found by assuming that the reason for the projection measurement errors δM_i were fluctuations of the true projection axis orientations $\boldsymbol{d}_i$ around the

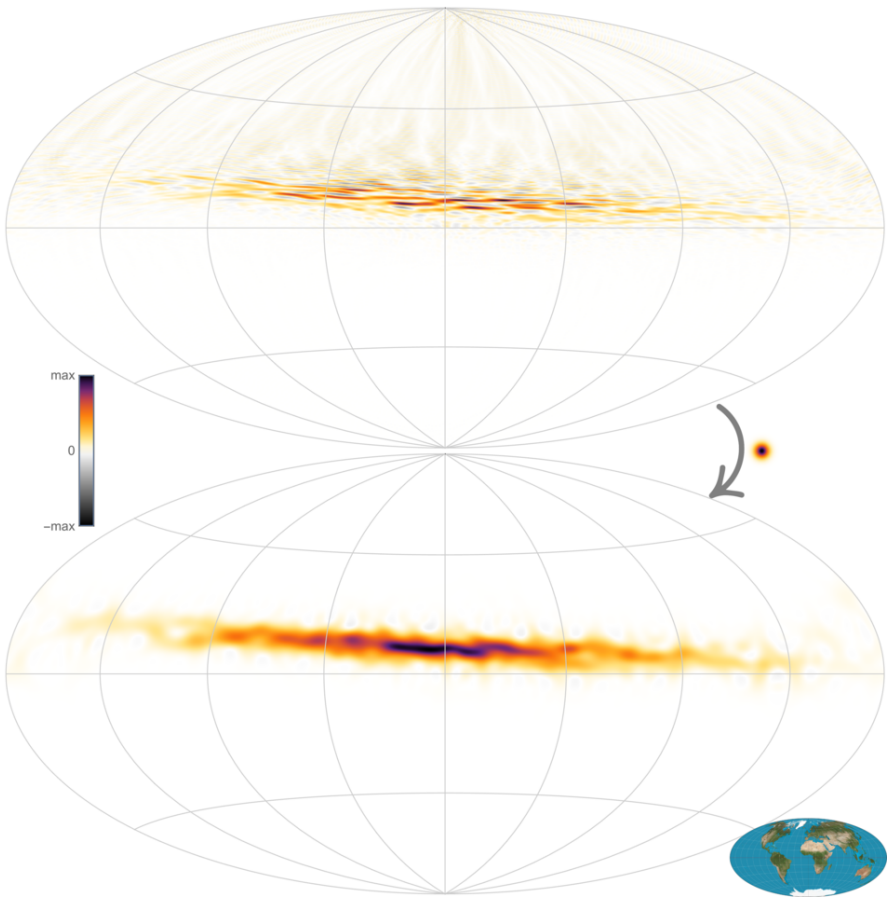

Figure 1.8: Example of a tomographically reconstructed density matrix of a system of $\bar{N} = 366$ atoms, determined from 16 143 projective measurements along many different axes. The resulting Wigner distribution [11] is shown in the Hammer projection (see the earth projection in the bottom-right panel [43]: equal-area; isotropic at the center). We recognize an over-squeezed spin state (see Figure 1.5). Top panel: The platonic Wigner distribution $W(\Theta, \Phi)$ as reconstructed by the $R\rho R$ algorithm. Bottom panel: The positivist Wigner distribution $W_g(\Theta, \Phi)$ after convolution with a Gaussian of angular spread $\sqrt{\langle[2\sin(\epsilon/2)]^2\rangle} \approx 2.5°$ (arrow), corresponding to $g = 524$ (see text and Figure 1.7). Data set 0000 from 20 November 2013.

desired orientations $\boldsymbol{d}_i^{(\text{ideal})}$, described by a Gaussian distribution of the angle $\epsilon = \cos^{-1}(\boldsymbol{d}_i \cdot \boldsymbol{d}_i^{(\text{ideal})})$ with zero mean and variance $\langle\epsilon^2\rangle \approx \langle[2\sin(\epsilon/2)]^2\rangle = 2 - 2\langle\boldsymbol{d}_i \cdot \boldsymbol{d}_i^{(\text{ideal})}\rangle$. Although this noise model is causally incorrect, it can reproduce the measured uncertainties in practice. We find that convolving

the Wigner distribution of a Dicke state $|\vartheta_i, \varphi_i, S_i, M_i\rangle$ with such a Gaussian (*i.e.* simulating the fluctuations of the Dicke-state projection axis) leads to a projection variance of $\langle \hat{S}^2_{\boldsymbol{d}_i}\rangle - \langle \hat{S}_{\boldsymbol{d}_i}\rangle^2 = \delta M_i^2 \approx [S_i(S_i+1) - M_i^2]/(2g)$ for large g. Using this relation we calculate an estimated smoothing angular momentum

$$\frac{1}{g} = \frac{1}{Q}\sum_{i=1}^{Q} \frac{2\delta M_i^2}{S_i(S_i+1) - M_i^2} \tag{1.32}$$

from the experimental data. Applying this smoothing ω_g to the Wigner distribution $W(\Theta, \Phi)$ of the platonic state (top panel of Figure 1.8), we find the positivist state $W_g(\Theta, \Phi) = (W * \omega_g)(\Theta, \Phi)$ [Equation (1.31)a] that represents our knowledge of the atomic state including measurement uncertainties (bottom panel of Figure 1.8). Idealized (noise-free) expectation values using this positivist state can reproduce our measurement data (see blue part of Figure 1.7).

Chapter 2

Quantum simulation of two-dimensional lattice systems

In this chapter I want to discuss briefly the progress that has come out of my foray into the quantum simulation of lattice models.

Two-dimensional lattice models are a critical test case for our understanding of quantum mechanics in general, and for specific theoretical descriptions used for their analysis. Since one-dimensional systems can usually be analyzed fully with the Jordan–Wigner transformation or the Bethe ansatz [44], and high-dimensional systems are well approximated by mean-field theories (often even exactly for $D \geq 4$), the two-dimensional case is in some ways the most critical setup. In a two-dimensional system, the number of each site's neighbors is large enough for complex correlations and long-range effects to be established, but small enough so that the site's individual behavior is not overwhelmed by its neighbors. Further, two-dimensional systems are experimentally much more accessible than higher-dimensional setups. My former Diploma student Philipp Hauke has summarized this situation very well in his PhD thesis [45].

In section 2.1 I briefly present a simple technique for analyzing two-dimensional lattice systems theoretically [9, 46]. Although I have not continued this theoretical work during my stay in Basel, my previous work on experimental implementations of such models has continued to grow. This work started with the invention of a powerful technique to find the globally optimal radio-frequency electrode shape for constructing a desired two-dimensional lattice of ion traps [47]. Briefly, this technique gives the definitive answer to the question of how to generate a desired three-dimensional electrostatic potential by setting up a two-dimensional surface electrode. Before this technique was invented, surface-electrode ion traps could only be constructed for particular situations of high symmetry, where the required shape of the radio-frequency electrode could be found intuitively (*e.g.* Figure 2.3). Now, optimal electrode shapes can be calculated with ease even for complicated trap setups (*e.g.* Fig-

ure 2.5), and their shapes turn out to be of a surprising beauty. The article presenting this technique has a high citation rate, and optimized surface-electrode ion traps are being constructed in several groups around the world [2, 48, 49]. Further, the generalization of this algorithm to the optimization of magnetic surface structures for generating two-dimensional lattices of atom traps [12] has spawned at least two experiments [50–52]. Most of these experimental implementations, as well as other works using two-dimensional surface electrodes [53–57], are based on the free software package called *SurfacePattern* that I have published online [10].

2.1 Modified spin-wave theory

Although modern computational techniques exist to approximate the ground state and (thermo-)dynamics of two-dimensional lattice models variationally, such as tensor networks [58], they all fail when the entanglement between distant lattice sites is too strong. As a result, the behavior of some extended two-dimensional quantum lattice models, such as the one developed in subsection 2.2.1, is still very difficult to simulate on a classical computer. This difficulty is one of the reasons why experimental implementations of such models, called quantum simulators, are of great interest, since they can determine model properties and dynamics that are out of reach for computer simulations.

However, even for complicated lattice models, the phase diagram is usually dominated by regions that can be simulated efficiently on a classical computer, often using methods as simple as mean-field theory. For those of us working in quantum technologies, it is easy to overlook how rare quantum systems are that cannot be simulated classically at all. To develop quantum simulators, we need a way of determining *a priori* which quantum systems hold any potential for representing a significant test case for our tools and methods. This is precisely what we have done in Refs. [9,46]; this work is still being pursued [59].

To illustrate this method, we briefly look at the spatially anisotropic triangular lattice (SATL) with XY interactions [46]. Its Hamiltonian

$$\hat{H} = \sum_{\langle ij \rangle} t_{ij} (\hat{S}_x^{(i)} \hat{S}_x^{(j)} + \hat{S}_y^{(i)} \hat{S}_y^{(j)}) \tag{2.1}$$

is shown schematically in Figure 2.1, with $t_{ij} = t_1$ for horizontal links, $t_{ij} = t_2$ for diagonal links, and $t_{ij} = 0$ for non-nearest-neighbors; the spin operators correspond to spins of any length S. The classical ($S \to \infty$) ground state can be studied with ease; but in the most quantum-mechanical case $S = 1/2$ even the zero-temperature quantum phase diagram contains speculative spin-liquid regions. This is due to the interplay between quantum fluctuations and frustration, which tends to require a fully quantum-mechanical treatment, particularly for small S.

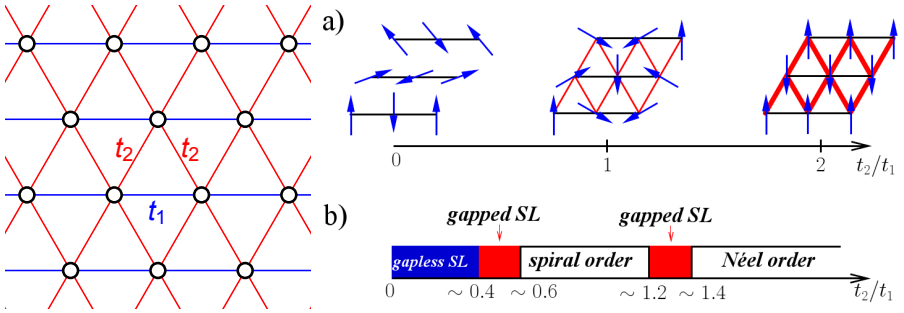

Figure 2.1: Left panel: Schematic representation of the spatially anisotropic triangular lattice with XY interactions, with spins located at the vertices (black circles). The Hamiltonian is given in Equation (2.1). Right panel (from Ref. [60]): (a) Classical zero-temperature spin ordering ($S \to \infty$, *i.e.* no quantum fluctuations): decoupled Néel-ordered horizontal (t_1) chains for $t_2/t_1 = 0$; three-sublattice spiral ordering for $t_2/t_1 = 1$; Néel order on the t_2 lattice for $t_2/t_1 \geq 2$. (b) Zero-temperature quantum phase diagram for $S = 1/2$; SL is short for spin liquid.

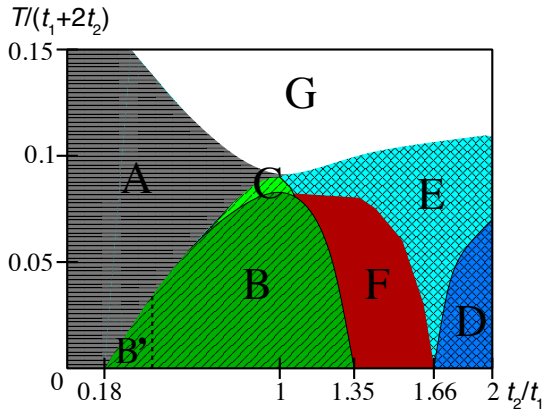

Figure 2.2: Schematic temperature-dependent phase diagram of the XY SATL, Figure 2.1, in terms of the anisotropy and the scaled temperature. Horizontal lines mark 1D-Néel order; diagonal lines spiral order; and cross-hatches 2D-Néel order. Phases A, C, and E are short-range ordered, *i.e.* exponential decay of correlations; phases B and D are quasi-long-range ordered, *i.e.* algebraic decay of correlations. The phase B' is believed to be a part of B. In regions F and G, the MSW formalism breaks down.

Takahashi's modified spin-wave (MSW) theory [61] describes each spin by

its fluctuations around the classical state found by taking the limit $S \to \infty$. These fluctuations are described by a Dyson–Maleev transformation, which is similar to the better-known Holstein–Primakoff transformation, and maps spin fluctuations to bosonic excitations. As in Ref. [62] we extend this method by optimizing the underlying classical state instead of using the $S \to \infty$ state, *i.e.* by minimizing the free energy of the system with respect to the underlying classical ordering vector. This extension yields a set of self-consistent equations that can be solved even for very large systems. However, they only have a meaningful solution on a subset of the possible system parameters. In particular, the method's breakdown in region F of Figure 2.2 indicates that the spin-liquid phase of the quantum phase diagram (bottom-right panel of Figure 2.1) may extend to finite temperatures. It is precisely this region F, singled out by the MSW theory with ordering vector optimization, where future quantum simulators are encouraged to study the spatially anisotropic triangular lattice; all other regions of the phase diagram do not require a description more sophisticated than a spin-wave theory.

2.2 SurfacePattern software

The design of surface-electrode ion traps and surface-magnetic atom traps requires that we can calculate the three-dimensional electromagnetic fields produced by such surface structures efficiently. In Ref. [63] I have described in detail how these calculations are done for surface electrodes giving rise to electric fields in space (including the leading-order effects of going beyond the approximation of a gapless infinite electrode plane); in Ref. [12] the same is done in less detail for magnetic surface structures. Although these references, and the works they are based on, offer a complete picture of the techniques to use, a practical computer implementation was called for in order to design ion and atom traps. Together with Janus Wesenberg, I have written a Mathematica package that offers this functionality in an efficient and easy-to-use form. This *SurfacePattern* package [10] allows the user to specify the shape of any two-dimensional electrode (or magnetized surface structure or wire loop, see subsection 2.2.4) by giving its outline as a polygonal shape, which may be finite or stretch to infinity. The package can then calculate the electrostatic potential, and its spatial derivatives, at any point in space.

To illustrate this in practice, we look at an example: we assume that an infinite grounded plane contains a square electrode at unit potential, located at $0 \leq x, y \leq 1$. We calculate the potential $V(x, y, z) =$ `V[x,y,z]` anywhere in three-dimensional space, as well as its spatial gradient $\nabla V(x, y, z) =$ `dV[x,y,z]`, with

```
In[1]:= Needs["SurfacePattern`"]      (double-click here to open source code)
In[2]:= P = PolygonPixel[{{0, 0}, {1, 0}, {1, 1}, {0, 1}}];
```

```
In[3]:= V[x_, y_, z_] = ComputeFinitePotential[0, P, {x,y,z}];
In[4]:= dV[x_, y_, z_] = ComputeFinitePotential[1, P, {x,y,z}];
```

The boundary condition on this potential is that $\lim_{z\to 0^+} V(x,y,z)$ is precisely the potential in the plane given by the square electrode:

$$\lim_{z\to 0^+} V(x,y,z) = V(x,y) = \begin{cases} 1 & \text{if } 0 < x < 1 \text{ and } 0 < y < 1, \\ 0 & \text{otherwise.} \end{cases} \tag{2.2}$$

Notice that we specify the polygonal electrode by a counter-clockwise list of points. For a polygon stretching to infinity, we use `InfPoint[a]` to specify a point in direction `a`, with `a` $= 0$ being in the x-direction, `a` $= \pi/2$ in the y-direction, etc. The potential of a semi-infinite strip electrode is thus defined with

```
In[5]:= Q = PolygonPixel[{InfPoint[0], {0, 1}, {0, 0}}];
In[6]:= W[x_, y_, z_] = ComputeFinitePotential[0, Q, {x,y,z}];
In[7]:= dW[x_, y_, z_] = ComputeFinitePotential[1, Q, {x,y,z}];
```

In the same way, spatial derivatives up to fifth order of the potentials generated by arbitrary polygonal electrodes, as well as circular disc electrodes, can be calculated with ease. This packaging of useful algorithms [64–66] has made calculations in the infinite gapless plane very practical. For example, the electrode shapes of Refs. [55, 57] and subsection 2.2.3 were found by optimizing a merit function (the pseudo-potential roughness in the electron- or ion-guiding channel) that was calculated as a function of the coordinates of the vertices of these electrode polygons. Such parametric optimizations can only be performed satisfactorily if the calculation of the merit function, and thus of the electrostatic potential throughout space, is very efficient for many different parameter sets (electrode shapes). Optimizing such shapes by traditional three-dimensional electrostatic solvers, which is many orders of magnitude slower, leads to sub-optimal results when the optimization cannot be converged fully [67].

In addition to these potential calculations, the *SurfacePattern* package contains the algorithm of Refs. [12, 47] that finds the globally optimal shapes of electrodes to achieve a desired three-dimensional field configuration. For this, the electrode is manually subdivided into a set of "pixel" electrodes, each of which will be either connected to unit potential or to ground; the algorithm's goal is to find the optimal pattern of these connections. The user specifies the values of the potential and its spatial derivatives at one or more points in three-dimensional space (or specifies `Automatic` if a value is unimportant and is allowed to take any value), and the algorithm finds the binary pixel potentials that maximize the numerical prefactor to these design constraints. In this way, the resulting pattern requires the least possible electrode voltage (or surface magnetization) to achieve the largest possible field values and derivatives. We

have found empirically that these binary patterns of pixel potentials are usually such that large areas of the surface are connected to the same potential; fine-structured or even fractal electrodes do not occur in this method. This makes the generated surface electrodes attractive for fabrication.

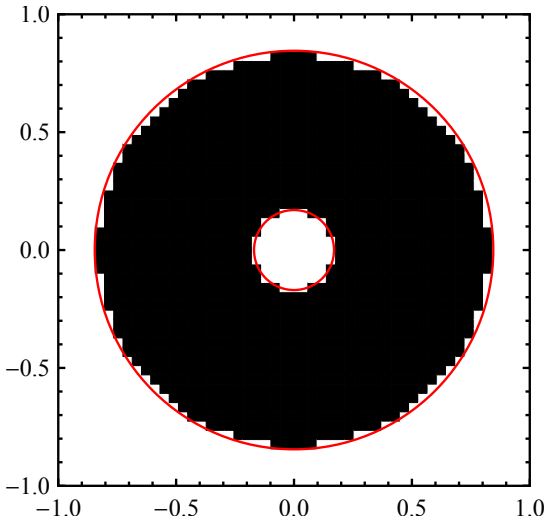

Figure 2.3: Optimized electrode calculated on a grid of 51×51 square pixels. Black pixels are connected to the rf voltage source, and white pixels are connected to ground, in order to generate the desired three-dimensional electrostatic potential for an ion trap at the point $(0, 0, 0.25)$. This shape matches the well-known optimal ring trap, whose circular edges are indicated with red circles [68].

As an example, we calculate the optimal radio-frequency surface electrode shape for a simple quadrupolar ion trap at the point $\boldsymbol{q} = (0, 0, 1/4)$ above the origin. We require that at the ion trap location, the three-dimensional electric potential has a zero gradient, $\nabla V(\boldsymbol{q}) = (0, 0, 0)$, and a quadrupolar curvature tensor proportional to $\left[\begin{smallmatrix} 1 & 0 & 0 \\ 0 & 1 & 0 \\ 0 & 0 & -2 \end{smallmatrix}\right]$, with the proportionality factor to be maximized by the algorithm. The value of the electric potential itself is not important (`Automatic`). To start, we limit the possible electrode shapes to the square $|x|, |y| \leq 1$, which we divide into 51×51 square pixels:

```
In[1]:= Needs["SurfacePattern`"]     (double-click here to open source code)
In[2]:= With[{d = 2/51},
          px = Flatten[Table[
            PolygonPixel[{{x,y}, {x+d,y}, {x+d,y+d}, {x,y+d}}],
            {x,-1,1-d,d}, {y,-1,1-d,d}]]];
```

For debugging, this set of pixels can be displayed with random coloring:

```
In[3]:= Graphics[{RandomColor[], PixelGraphics[#]} & /@ px, Frame -> True]
```

The optimal configuration is calculated with

```
In[4]:= opt = OptimalFinitePattern[px,
          {{{0, 0, 0.25},
            Automatic,
            {0, 0, 0},
            {{1,0,0},{0,1,0},{0,0,-2}}}}];
```

which specifies the constraints on the three-dimensional potential at the point $\boldsymbol{q}$. The output variable `opt[[1]]` now holds a list of potentials to be applied to the 2601 pixels, which we show in Figure 2.3 with

```
In[5]:= Graphics[MapThread[{GrayLevel[1-#2],PixelGraphics[#1]}&,
          {px, opt[[1]]}], Frame -> True]
```

The resulting three-dimensional potential and its spatial derivatives are computed with

```
In[6]:= V[x_, y_, z_] = opt[[1]].
          (ComputeFinitePotential[0, #, {x, y, z}]& /@ px);
In[7]:= dV[x_, y_, z_] = opt[[1]].
          (ComputeFinitePotential[1, #, {x, y, z}]& /@ px);
In[8]:= ddV[x_, y_, z_] = opt[[1]].
          (ComputeFinitePotential[2, #, {x, y, z}]& /@ px);
```

We find, as desired, that `dV[0,0,0.25]={0,0,0}`. Further, we find that the curvature tensor at the point $\boldsymbol{q}$, calculated with `ddV[0,0,0.25]`, is 3.76291 times the desired curvature tensor. This maximized prefactor, given in `opt[[2]]`, is only 0.5% below the analytic value for a fully optimized ring trap [68] (red circles in Figure 2.3).

Aside from finite pattern calculations and optimizations, the *SurfacePattern* package can also deal with infinite two-dimensional patterns. In general, these patterns are set up in the $p1$ wallpaper group by subdividing a parallelogram-shaped unit cell, defined by two lattice vectors, into $n \times n$ parallelogram-shaped "pixels". Examples of such calculations are given below in subsection 2.2.1 and subsection 2.2.4.

With calculations of this kind, and the examples on the website of Ref. [10], many design problems of practical relevance can be tackled, especially in situations where we have no intuitive way of determining the shape of an electrode for given design constraints. In what follows I briefly present several such results.

2.2.1 infinite pattern: the Kitaev honeycomb model [8]

In 2006 Alexei Kitaev presented the first exactly solvable model of a two-dimensional spin-1/2 lattice system with a topologically non-trivial ground state (a "toric code") [69]. Very briefly, what this means is that the excitations of this system are Abelian or non-Abelian anyons, depending on coupling strengths. These excitations lie at the center of topological quantum computing, where entangling operations consist of spatially moving ("braiding") such anyons around each other.

The top panel of Figure 2.4 shows the Hamiltonian of the Kitaev honeycomb model graphically. In Ref. [8] we have proposed a concrete implementation of this Hamiltonian, based on a carefully crafted two-dimensional array of trapped ions, shown in the bottom panels of Figure 2.4. The core of this implementation is the realization that the effective couplings between the internal states of the ions can be approximately proportional to the dipole–dipole vibrational couplings between the ions' spatial motions. If the principal axes of vibrations of ions in a honeycomb lattice are chosen correctly, then these dipole–dipole couplings can represent approximately the desired link-specific couplings of the Kitaev model. These principal axes of vibration, and their associated pseudo-potential curvatures, serve as inputs into a surface-electrode optimization carried out with *SurfacePattern*. We find a structure that satisfies all of these constraints, shown in Figure 2.4 (bottom right panel). Connecting this blue electrode to a radio-frequency source would generate the desired three-dimensional trap structure, which, when populated with a single ion per trap and driven magnetically, would approximate the physics of the Kitaev model.

To date, this proposal has not been implemented. However, the work of the following subsection 2.2.2 represents a first step in exactly this direction.

Mathematica code

Here we calculate the surface electrode pattern of Figure 2.4 (bottom-right panel). First, we load the *SurfacePattern* package:

```
In[1]:= Needs["SurfacePattern`"]     (double-click here to open source code)
```

The calculation is done on an infinite hexagonal lattice whose basis vectors are, in units of the inter-ion spacing,

```
In[2]:= lattice = {{Sqrt[3], 0}, {Sqrt[3]/2, 3/2}};
```

Within each unit cell of this lattice there are two ion traps located at height `h` above the chip, and with Cartesian coordinates given by `P1` and `P2`:

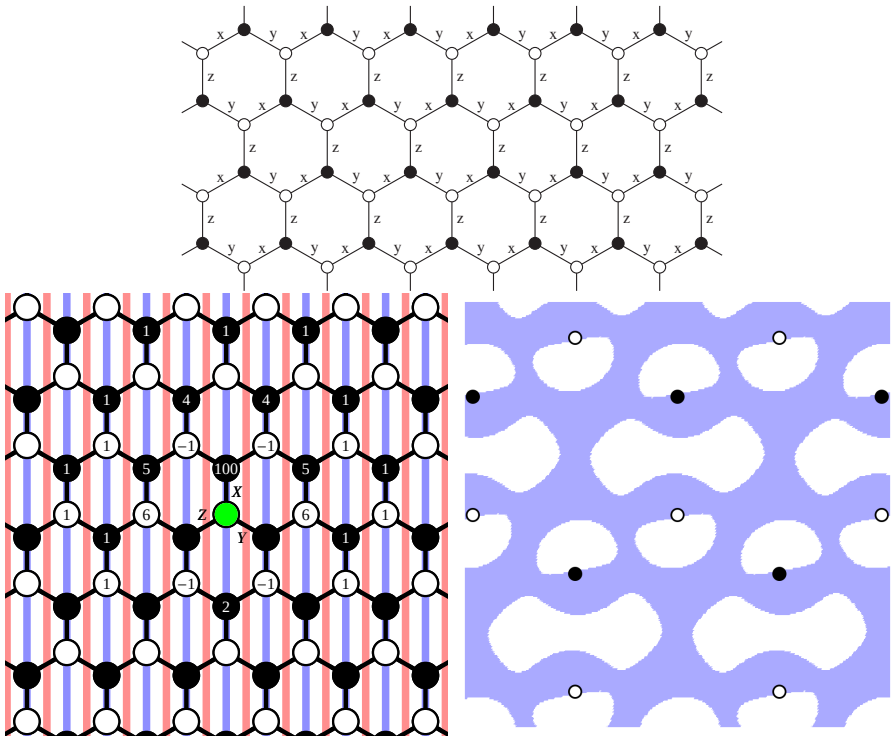

Figure 2.4: Top panel: Graphical representation of the Kitaev honeycomb model, taken from Ref. [69]. The Hamiltonian is $\hat{H} = -J_x \sum_{x\text{-links}} \hat{\sigma}_x^{(j)} \hat{\sigma}_x^{(k)} - J_y \sum_{y\text{-links}} \hat{\sigma}_y^{(j)} \hat{\sigma}_y^{(k)} - J_z \sum_{z\text{-links}} \hat{\sigma}_z^{(j)} \hat{\sigma}_z^{(k)}$, constructed from three different link types and two different site types. Bottom left panel: Our proposed implementation of this Hamiltonian with a two-dimensional lattice of trapped ions. The interaction of the vibrational motion of the green ion with its neighbors, mediated by the Coulomb interaction, is shown exemplarily for the X-link component, which is strongest (100%) along the X-direction, vanishes along the Y- and Z-directions, and remains at 6% or lower for all other directions. Red and blue lines represent wires carrying radio-frequency currents for driving these couplings magnetically. Couplings along the Y- and Z-links are established by rotating this pattern by $\pm 120^\circ$ and shifting the magnetic drive frequency. Bottom right panel: Surface radio-frequency electrode (blue) and dc electrodes (white) that generate a honeycomb lattice of ion traps with the desired principal directions of vibration that lead to the couplings of the bottom left panel. The trapping height is half the inter-ion spacing.

```
In[3]:= h = 1/2;
In[4]:= P1 = {0, 0, h};
```

```
In[5]:= P2 = {Sqrt[3], 1, h};
```

The principal axes of vibration (curvature) at the microtrap sites, in Cartesian coordinates, corresponding to the three types of couplings:

```
In[6]:= m1X = {1/Sqrt[2], 1/Sqrt[6], -1/Sqrt[3]};
In[7]:= m1Y = {1/Sqrt[2], -1/Sqrt[6], 1/Sqrt[3]};
In[8]:= m1Z = {0, -Sqrt[2/3], -1/Sqrt[3]};
In[9]:= m2X = {-1/Sqrt[2], -1/Sqrt[6], -1/Sqrt[3]};
In[10]:=m2Y = {-1/Sqrt[2], 1/Sqrt[6], 1/Sqrt[3]};
In[11]:=m2Z = {0, Sqrt[2/3], -1/Sqrt[3]};
```

These directions have been chosen such that the resulting dipole–dipole couplings, shown in Figure 2.4 (bottom-left panel), approximate the Kitaev Hamiltonian. For each microtrap, in the local coordinate system spanned by these three principal axes of vibration, the curvature tensor of the rf electric field is such that the three vibrational eigen-frequencies of the trapped ion's motion are as far from each other as possible, while fulfilling the sum rule of a traceless curvature tensor:

```
In[12]:=curvature = {{1/GoldenRatio, 0, 0},
                     {0, 1, 0},
                     {0, 0, -GoldenRatio}};
```

Find the optimal periodic pattern that satisfies the above constraints, subdividing the unit cell of the lattice into `n` × `n` pixels:

```
In[13]:=n = 50;
In[14]:=opt = OptimalPeriodicPattern[lattice, n,
         {{{P1, Transpose[{m1X, m1Y, m1Z}]},
            Automatic, {0, 0, 0}, curvature},
          {{P2, Transpose[{m2X, m2Y, m2Z}]},
            Automatic, {0, 0, 0}, curvature}}, {}];
```

Make a plot of the optimal pattern in a finite region (bottom-right panel of Figure 2.4):

```
In[15]:=s = 2;
In[16]:=PlotPeriodicPattern[opt, {{-s, s, Sqrt[3]/n}, {-s, s, Sqrt[3]/n}}]
```

We compute the `d`th spatial derivative tensor of the three-dimensional potential generated at $\boldsymbol{r} = \{\mathtt{x}, \mathtt{y}, \mathtt{z}\}$ by this optimized electrode pattern ($\mathtt{d} \in \{0, 1, 2, 3\}$) with

```
In[17]:=V[d_, {x_, y_, z_}] :=
         ComputePeriodicPotential[d, lattice, {x, y, z}, opt[[1]]]
```

From this, the ponderomotive pseudo-potential can be calculated with

```
In[18]:=W[x_, y_, z_] := #.#& @ V[1, {x, y, z}]
```

2.2.2 finite pattern: the cloverleaf traps [2]

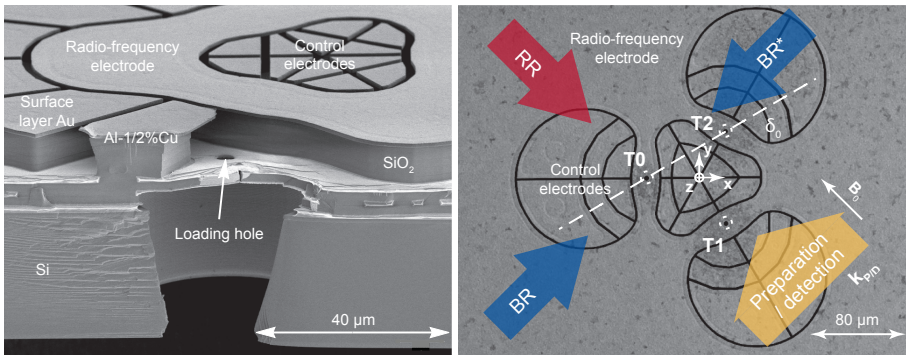

Figure 2.5: Surface-electrode ion trap featuring three individual traps, from Ref. [2]. Left panel: Scanning electron microscope (SEM) image of a cleaved copy of the chip. It provides a cross-sectional view vertically through the trap chip (bottom half of image) and a top view of the horizontal, planar trap electrode surface (top half of image) of the 40 μm array. Buried electrode interconnects as well as the overhangs of electrodes that shield trapped ions from insulating surfaces are exposed in this view. A loading channel, vertically traversing the chip, collimates a neutral atom beam from an oven on the backside of the chip. Right panel: SEM top-view of the 80 μm array, dark lines indicate gaps between individual electrodes and dashed circles highlight the three trap sites at **T0**, **T1**, and **T2** that lie 40 μm above the electrode plane; corresponding loading holes appear as dark spots. A vertical plane connecting **T0** and **T2** is shown as a dotted line and labelled with δ_0. The single RF electrode extends beyond the image area and encloses 30 control electrodes grouped into four islands depicted in the central part of the image, enabling the control of individual trap sites (see Figure 2.6). Laser beams (coloured arrows) are parallel to the chip surface and wave vectors $\boldsymbol{k}_{\mathrm{P/D}}$ of preparation and detection beams are parallel to the magnetic quantisation field $\boldsymbol{B}_0$ (white arrow).

The first experimental step towards two-dimensional lattice models like the Kitaev honeycomb model (subsection 2.2.1) has been taken recently in Tobias Schätz's group [2]. In this work, two radio-frequency surface electrodes were designed to generate three equidistant ion traps each, spaced by either 40 μm or 80 μm, localized 40 μm above the electrode plane. These surface electrodes have been fabricated with the utmost precision at Sandia National Laboratories as multi-layer under-etched sandwich structures, including localized holes for back-side loading, as shown in Figure 2.5.

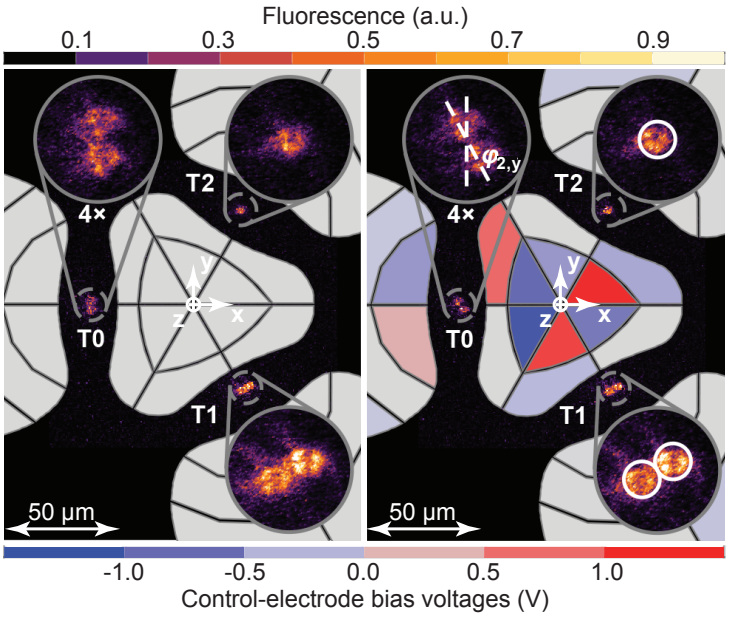

Figure 2.6: Individual control of mode orientations in the 80 μm chip (right panel of Figure 2.5). EMCCD images of pairs of ions near **T0** and **T1**, and a single ion near **T2** (insets are magnified four-fold). The dc control electrodes are colored in the right image according to their bias voltage v_j (see text). Ion pairs align along $\boldsymbol{u}_2$, the lowest-frequency vibrational mode in the local trap. The left image captures ion positions for $U_{\text{rot}} = 0\,\text{V}$, and $\omega_2 = 2\pi \times 1.9(2)\,\text{MHz}$ near **T0**. The right image illustrates the rotation effect for $U_{\text{rot}} = 2.45\,\text{V}$: mode $\boldsymbol{u}_2$ near **T0** with $\omega_2 = 2\pi \times 1.8(2)\,\text{MHz}$ is rotated by $\varphi_{2,\text{y}} = 31(5)^\circ$, whereas ion positions near **T1** and **T2** remain unchanged; white circles indicate initial ion positions (for $U_{\text{rot}} = 0\,\text{V}$).

Ions were successfully trapped in all rf microtraps, as shown in Figure 2.6 for the 80 μm chip. As in every ion-trap experiment, it is crucial to be able to control the position and principal axes of vibrational motion of every ion trap separately, in order to (i) compensate for fabrication inaccuracies and stray electric fields and (ii) tune the traps into particular resonances with each other, to generate the desired dipolar (vibrational) couplings [8]. Each ion trap has eight degrees of freedom that can be tuned independently: the three spatial coordinates of its minimum location and the five degrees of freedom of the curvature tensor of the radio-frequency electric field at the minimum.[1] For an array of three ion traps, 24 degrees of freedom need to be controlled with at least 24 dc electrodes whose potentials can be set independently. The

[1] The curvature tensor of the electric field is a symmetric 3×3 matrix with zero trace.

designs of Ref. [2] include 30 such control electrodes for additional flexibility.

In the right panel of Figure 2.6 an example of the use of these control electrodes is shown. We design a voltage pattern $\boldsymbol{v}$ such that the jth control electrode is set to $U_j = U_{\text{rot}} \times v_j$, where U_{rot} is an overall voltage prefactor and v_j are numerical coefficients with $\|\boldsymbol{v}\| = 1$. This voltage pattern $\boldsymbol{v}$ is calculated such that the ion positions of all three traps and the ion trap curvatures of traps **T1** and **T2** do not change with U_{rot}, and such that the curvature tensor of trap **T0** is rotated in the xy-plane as sensitively as possible with U_{rot}. The figure shows the control electrodes colored according to their coefficients v_j. The experimental work of Figure 2.6 demonstrates that the construction and individual control of our designed ion microtraps is possible. In the future, larger arrays in the spirit of subsection 2.2.1 will be attempted.

Mathematica code

The Mathematica code to calculate the 80 μm cloverleaf electrode shape (Figure 2.6 and right panel of Figure 2.5) is given as an example on the web site of Ref. [10]. Here I give a minimal version of this code.

First, we load the *SurfacePattern* package:

```
In[1]:= Needs["SurfacePattern`"]     (double-click here to open source code)
```

We will do the pattern optimization over a finite hexagonal region of unit size around the origin, to respect the symmetry of the setup. This region is subdivided into $3\mathtt{n}^2 + 3\mathtt{n} + 1$ hexagonal pixels:

```
In[2]:= n = 50;
In[3]:= px = Flatten[Table[PolygonPixel[
          Table[({i+j/2, j*Sqrt[3]/2} + {Cos[p], Sin[p]}/Sqrt[3])/(n+1/2),
            {p, Pi/6, 2Pi, Pi/3}]],
          {i, -n, n}, {j, -n-Min[0,i], n-Max[0,i]}]];
```

For debugging, this set of pixels can be displayed with random coloring:

```
In[4]:= Graphics[{RandomColor[], PixelGraphics[#]} & /@ px, Frame -> True]
```

There will be three traps arranged in an equilateral triangle, parametrized by the angle $\mathtt{p} \in \{0, 2\pi/3, 4\pi/3\}$. For the trap at angle `p`, the trapping conditions are given by `P[p]`, containing the Cartesian coordinates of the trap position, the three principal axes of curvature of the trap, and the conditions on the electric field at the trap location (zero of the gradient; quadrupolar confinement in the frame of the principal axes):

```
In[5]:= h = 1/8;  (* trapping height *)
In[6]:= f = 2*h;  (* inter-trap distance *)
In[7]:= P[p_] = {{{f*Cos[p]/Sqrt[3], f*Sin[p]/Sqrt[3], h},
```

```
        Transpose[{{-Sin[p]/Sqrt[2], Cos[p]/Sqrt[2], -1/Sqrt[2]},
                   {-Sin[p]/Sqrt[2], Cos[p]/Sqrt[2], 1/Sqrt[2]},
                   {Cos[p], Sin[p], 0}}]},
        Automatic, {0, 0, 0}, {{1, 0, 0}, {0, 1, 0}, {0, 0, -2}}};
```

The curvature tensor is thus a symmetric quadrupole with the stiff axis being the radial direction (outward from the array's center of symmetry), whereas the two perpendicular directions are the soft axes.

The optimal pattern of connections to the rf source is found with

```
In[8]:= opt = OptimalFinitePattern[px, Table[P[p], {p, 0, 4Pi/3, 2Pi/3}]];
```

We show this optimal pattern such that the rf electrode appears in black:

```
In[9]:= Graphics[Transpose[{GrayLevel[1-#]&/@opt[[1]], PixelGraphics[px]}],
        Frame -> True]
```

We compute the `d`th spatial derivative tensor of the three-dimensional potential generated at $\boldsymbol{r} = \{\mathtt{x}, \mathtt{y}, \mathtt{z}\}$ by this optimized electrode pattern ($\mathtt{d} \in \{0, 1, 2, 3, 4, 5\}$) with

```
In[10]:=V[d_, {x_, y_, z_}] :=
        opt[[1]].(ComputeFinitePotential[d, #, {x, y, z}] & /@ px)
```

From this, the ponderomotive pseudo-potential can be calculated with

```
In[11]:=W[x_, y_, z_] := #.#& @ V[1, {x, y, z}]
```

2.2.3 switchable Y-junction for ion shuttling

The long-term goal of research into quantum information processing (QIP) is the construction of a quantum computer [70]. At the present time, there are several promising architectures for constructing such a device, where long coherence times are matched by fast and reliable one- and two-qubit gates. Nonetheless, to date no QIP device can be scaled to a size where it can start answering open questions about complex systems.

One of the systems where high-fidelity two-qubit quantum gates have been demonstrated is trapped ions [71, 72]. It has been suggested that these gates could be assembled into a fault-tolerant quantum computer if the ions could be shuttled through space without losing their coherence [73], essentially transporting quantum information between different interaction regions. Ion shuttling along channels and through X-intersections has already been demonstrated with high fidelity [74].

We have designed a switchable Y-intersection where an ion can be shuttled from one channel to any of two others (Figure 2.7). The idea was to have

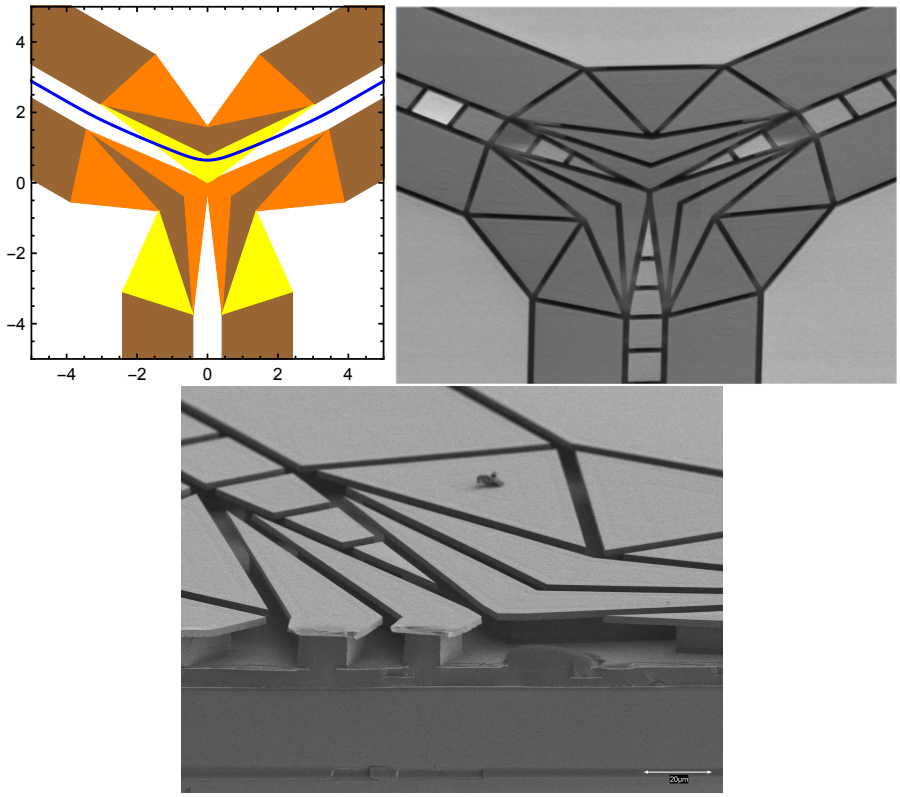

Figure 2.7: Switchable Y-junction between three ion channels. Top left: *SurfacePattern* simulation involving always-on rf electrodes (brown) and switchable rf electrodes that are currently on (orange) or grounded (yellow). In this configuration, an ion guiding channel is generated that connects the upper-left to the upper-right corner through a 60° turn (blue line, at unit height above the chip surface). Top right: SEM image of this pattern fabricated by Sandia National Labs, including dc control electrodes. Bottom: SEM closeup of a section of a failed chip, showing the under-etched electrodes and the vertical interconnects in the multi-layer structure, similar to the left panel of Figure 2.5. In this elegant chip, the trapped ions never "see" the dielectric insulator pillars below the electrodes, and the bottom of the gaps between the electrodes is a grounded plane.

nine switchable electrodes that could be either connected to the same radio-frequency voltage source as the straight electrodes forming the ion channels, or connected to ground (or any dc voltage for additional control). For a fixed setting of the switches, the electrodes would generate a smooth ion guiding channel from one arm of the chip to another arm, without encountering any

pseudopotential bumps. The ion would be confined at all times while passing the intersection, instead of going ballistically through an unconfined region as in static X- or Y-intersections [75]. The Mathematica code for calculating the rf electric field of this electrode is given as an example on the web site of Ref. [10].

This design was fabricated with extreme care at Sandia National Labs as a multi-layer chip with several conducting planes and vertical interconnects (see Figure 2.7).

2.2.4 periodic Ioffe–Pritchard atom trap arrays

According to Maxwell's equations, both the electric field $\boldsymbol{E}$ and the magnetic field $\boldsymbol{B}$ are divergence-free in free space (in the absence of charges and currents, respectively), and can therefore be written as the gradients of scalar fields. For the electric field, we write $\boldsymbol{E} = -\nabla\Phi$ in terms of the electric potential Φ; by analogy, the magnetic field can be written as $\boldsymbol{B} = -\nabla\Psi$ in terms of the scalar magnetic potential Ψ (to be distinguished from the vector potential $\boldsymbol{A}$ for which $\boldsymbol{B} = \nabla \times \boldsymbol{A}$). These potentials thus both satisfy Laplace's equation in free space: $\nabla^2\Phi = \nabla^2\Psi = 0$. The boundary condition of the electric potential is determined by the electric potentials of the surface electrodes (see section 2.2); similarly, the boundary condition of the scalar magnetic potential is set by the out-of-plane surface magnetization [12]. Since this surface magnetization can be set by depositing and patterning a ferromagnetic thin film on a non-magnetic substrate, the optimized surface patterns of section 2.2 can be used to design and generate almost arbitrary magnetic fields in three-dimensional space. Alternatively, a current-carrying wire tracing the outlines of these magnetized regions counter-clockwise generates the same magnetic field (via the Stokes theorem).

In Ref. [12] we have used this method to calculate the optimal binary two-dimensional pattern of surface magnetization that would generate a square lattice of Ioffe–Pritchard atom traps. This pattern, shown in the top left panel of Figure 2.8, was fabricated at several length scales at the universities of Amsterdam and the Negev, for trap separations from 100 nm to 10 μm [51, 76]. In all samples, thin iron-platinum (FePt) films were patterned to the desired shape using lithographic techniques, then magnetized permanently in a strong field perpendicular to the surface. Then, by applying a much weaker homogeneous bias field (the Ioffe field), these magnetic surface patterns generate two-dimensional arrays of identical Ioffe–Pritchard atom traps. The bottom panel of Figure 2.8 shows an absorption image of ^{87}Rb atoms loaded into these traps. The goal of these experiments is to build two-dimensional atom trap lattices as a platform for two-dimensional lattices of quantum information carriers.

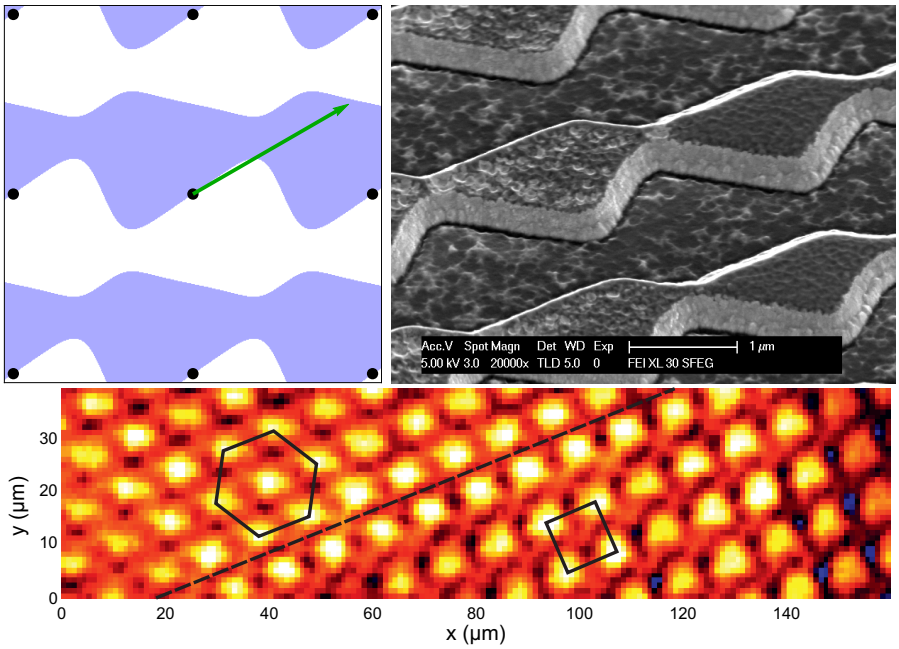

Figure 2.8: Square lattice of Ioffe–Pritchard traps. Top panels: Optimized magnetization pattern and Ioffe axis (left) and SEM image of the micro-fabricated FePt surface structure fabricated at 1 μm trap separation (right). Bottom panel: Absorption image showing rubidium atoms loaded simultaneously into hexagonal (left side) and square (right side) lattices with a 10 μm trap separation. The dotted line denotes the interface, where there is a crossover between the two geometries. From Refs. [51, 76].

Chapter 3

Teaching practical quantum mechanics on a computer

When I first learned quantum mechanics at several universities, we were taught the basic notations and core principles, and proceeded to solve every analytically solvable model over and over again (square well, harmonic oscillator, gravity well, hydrogen atom). These models are so specialized and have so little to do with what I knew about the mechanics of the human world, that it took me a very long time after my diploma degree to develop an intuitive understanding of quantum mechanics and to begin to see how to apply it to problems I knew well from classical mechanics. My graduate studies in Physical Chemistry at Princeton University helped greatly in this development, since the quantum-mechanical description of molecular structures and dynamics is within reach of the intuition of a graduate student. My post-doctoral stay in Ignacio Cirac's theory group at the Max Planck Institute of Quantum Optics allowed me to diversify and solidify this knowledge. In this way, over the years, I was able to integrate quantum mechanics into my view of how the world can be described at a practical level.

Remembering the difficulties I encountered and the frustrating opaqueness of the path between quantum-mechanics courses, on the one hand, and full-fledged descriptions of real-world systems, on the other, I decided in 2012 to offer a weekly lecture at the University of Basel that would plow this path for advanced physics students. My vision was to enable them to take what they have learned in previous lectures and start applying their tools to more complex and more interesting systems. Naturally, none of these more complex systems can be described in the paper-and-pencil analytical ways that homework problems of undergraduate quantum-mechanics lectures can; and so I decided to offer an *Introduction to Computational Quantum Mechanics*. Although the course is taught in the Mathematica programming system, its concepts and tools can be transferred to any programming language. I have offered this lecture in the Fall of 2012 and 2013, as well as in the Spring of 2015 and

2016.

The goal of this lecture is to take the students after several undergraduate lectures on quantum mechanics and show them some of the possibilities of the quantum-mechanical description of our world. Although the lecture presents many tools and insights, the students are expected to propose and complete an individual project where they apply these tools to a problem of their choice. My hope is to encourage the students to find their own questions and to delve deeply into a particular problem, which will change their view of quantum mechanics and allow them to build confidence for using their skill and intuition in their future research.

The lecture script is published on the arXiv [6] with the goal of reaching a larger audience throughout the world, particularly in places where advanced quantum-mechanics lectures cannot be found. Because of its length, only its introduction is included in this document.

Acknowledgments

The work presented here has been initiated and supported by many people, to whom I am very grateful. For me, working as a research scientist has always been about being influenced by other people, and influencing them in turn. Together we create the fertile mental soil in which new ideas, concepts, even paradigms can germinate and grow.

Almost none of the work presented in this document would have been possible without the excellent presence and leadership of **Philipp Treutlein**. His unassuming guidance is for me the embodiment of Lao-tzu's Master [77]:

> The Master doesn't talk, he acts.
> When his work is done,
> the people say, "Amazing:
> we did it, all by ourselves!"

I am grateful to **Pascal Böhi** and **Max Riedel** for introducing me to the BEC machine with which we measured Refs. [1, 7]. They have done an impressive job in building this machine, and their patience in explaining its functions to Caspar and me has been astonishing.

I want to express my gratitude to **Caspar Ockeloen**, **Baptiste Allard**, and **Matteo Fadel**, with whom it has been a pleasure to work both in the lab and in the office. Thank you for forming a relaxed and productive setting in which we can all contribute freely without stepping on each other's feet.

The work on Ref. [1] would not have been possible without the initiative and persistence of **Jean-Daniel Bancal** and **Nicolas Sangouard**. Their optimism for finding an experimentally feasible Bell correlation witness has been a continuous source of inspiration; none of us on the experimental side would have thought that this goal could be reached, and we had to be intiated with much patience to this topic.

Further thanks go to the rest of the Treutlein and Sangouard groups in Basel: **Aline Faber**, **Andreas Jöckel**, **Andrew Horsley**, **Enky Oudot**, **Gianni Buser**, **Guan-Xiang Du**, **Janik Wolters**, **Lucas Béguin**, **Maria Korppi**, **Matthew Rakher**, **Melvyn Ho**, **Michael Zwerger**, **Thomas Karg**, **Tilman Zibold**, and **Tobias Kampschulte**.

I would like to thank **Didi Leibfried** for inviting me to work at NIST Boulder in 2010. This brief stay, initiated by our joint work on Refs. [12, 47], has

generated Refs. [2, 8, 10], and the beauty and comfort of the city of Boulder and its people have made a lasting impression on me.

Finally I want to express my deep gratitude to **Vanessa Leung**, whose work [50, 51, 76] has brought our lives together. Your presence sets me free.

Bibliography

[1] Roman Schmied, Jean-Daniel Bancal, Baptiste Allard, Matteo Fadel, Valerio Scarani, Philipp Treutlein, and Nicolas Sangouard. Bell correlations in a Bose-Einstein condensate. *Science*, 352(6284):441–444, 2016. 3, 4, 5, 9, 12, 19, 20, 21, 51, 61, 85, 86

[2] Manuel Mielenz, Henning Kalis, Matthias Wittemer, Frederick Hakelberg, Ulrich Warring, Roman Schmied, Matthew Blain, Peter Maunz, David L. Moehring, Dietrich Leibfried, and Tobias Schaetz. Arrays of individually controlled ions suitable for two-dimensional quantum simulations. *Nat. Commun.*, 7, Jun 2016, http://doi.org/10.1038/ncomms11839. 4, 5, 32, 41, 43, 52, 61

[3] Baptiste Allard, Matteo Fadel, Roman Schmied, and Philipp Treutlein. Sideband Rabi spectroscopy of finite-temperature trapped Bose gases. *Phys. Rev. A*, 93:043624, Apr 2016. 4, 5, 9, 62

[4] Roman Schmied. Quantum state tomography of a single qubit: comparison of methods. *J. Mod. Opt.*, 63(18):1744–1758, 2016. 4, 5, 21, 22, 28, 62

[5] Florian Fröwis, Roman Schmied, and Nicolas Gisin. Tighter quantum uncertainty relations following from a general probabilistic bound. *Phys. Rev. A*, 92:012102, Jul 2015. 4, 5, 21, 63

[6] Roman Schmied. Lecture script: Introduction to computational quantum mechanics. 2014, arXiv:1403.7050 [quant-ph]. 4, 5, 50, 61, 63

[7] Caspar F. Ockeloen, Roman Schmied, Max F. Riedel, and Philipp Treutlein. Quantum metrology with a scanning probe atom interferometer. *Phys. Rev. Lett.*, 111:143001, Oct 2013. 4, 5, 8, 9, 15, 17, 19, 21, 51, 64

[8] Roman Schmied, Janus H. Wesenberg, and Dietrich Leibfried. Quantum simulation of the hexagonal Kitaev model with trapped ions. *New J. Phys.*, 13(11):115011, Nov 2011. 4, 5, 38, 42, 52, 64

[9] Philipp Hauke, Tommaso Roscilde, Valentin Murg, J. Ignacio Cirac, and Roman Schmied. Modified spin-wave theory with ordering vector optimization: spatially anisotropic triangular lattice and $J_1 J_2 J_3$ model with Heisenberg interactions. *New J. Phys.*, 13(7):075017, Jul 2011. 4, 5, 31, 32, 65

[10] Roman Schmied. SurfacePattern: a Mathematica package for surface atom and ion traps, 2011-2016. https://atom.physik.unibas.ch/people/romanschmied/code/SurfacePattern.php. 4, 5, 32, 34, 37, 43, 46, 52, 61, 65

[11] Roman Schmied and Philipp Treutlein. Tomographic reconstruction of the Wigner function on the Bloch sphere. *New J. Phys.*, 13(6):065019, Jun 2011. 4, 5, 13, 21, 22, 25, 29, 66

[12] Roman Schmied, Dietrich Leibfried, Robert J. C. Spreeuw, and Shannon Whitlock. Optimized magnetic lattices for ultracold atomic ensembles. *New J. Phys.*, 12(10):103029, Oct 2010. 4, 5, 32, 34, 35, 46, 51, 66

[13] Alfred Korzybski. *Science and Sanity: An Introduction to Non-Aristotelian Systems and General Semantics*. Institute of General Semantics, Brooklyn, USA, fifth edition, 2000. 5

[14] Masahiro Kitagawa and Masahito Ueda. Squeezed spin states. *Phys. Rev. A*, 47:5138–5143, Jun 1993. 8, 13, 15

[15] Daniel A. Steck. Rubidium 87 D line data. Available online at http://steck.us/alkalidata, revision 2.1.5, 13 January 2015. 8, 10

[16] Anthony J. Leggett. Bose-Einstein condensation in the alkali gases: Some fundamental concepts. *Rev. Mod. Phys.*, 73:307–356, Apr 2001. 9

[17] W. Ketterle, D. S. Durfee, and D. M. Stamper-Kurn. Making, probing and understanding Bose-Einstein condensates. 1999, arXiv:cond-mat/9904034. 9

[18] Philipp Treutlein. *Coherent manipulation of ultracold atoms on atom chips*. PhD thesis, Ludwig–Maximilians–Universität München, 2008. 9

[19] Pascal A. Böhi. *Coherent manipulation of ultracold atoms with microwave near-fields*. PhD thesis, Ludwig–Maximilians–Universität München, 2010. 9, 13

[20] Max F. Riedel. *Multi-particle entanglement on an atom chip*. PhD thesis, Ludwig–Maximilians–Universität München, 2010. 9, 13

[21] Caspar F. Ockeloen. *Quantum Metrology with a Scanning Probe Atom Interferometer*. PhD thesis, University of Basel, 2014. 9, 13

[22] Pascal Böhi, Max F. Riedel, Johannes Hoffrogge, Jakob Reichel, Theodor W. Hänsch, and Philipp Treutlein. Coherent manipulation of Bose-Einstein condensates with state-dependent microwave potentials on an atom chip. *Nat. Phys.*, 5(8):592–597, 08 2009. 9, 14

[23] Max F. Riedel, Pascal Böhi, Yun Li, Theodor W. Hänsch, Alice Sinatra, and Philipp Treutlein. Atom-chip-based generation of entanglement for quantum metrology. *Nature*, 464(7292):1170–1173, 04 2010. 9, 14, 19, 66

[24] C. Deutsch, F. Ramirez-Martinez, C. Lacroûte, F. Reinhard, T. Schneider, J. N. Fuchs, F. Piéchon, F. Laloë, J. Reichel, and P. Rosenbusch. Spin self-rephasing and very long coherence times in a trapped atomic ensemble. *Phys. Rev. Lett.*, 105:020401, Jul 2010. 10

[25] Walther Gerlach and Otto Stern. Der experimentelle Nachweis der Richtungsquantelung im Magnetfeld. *Z. Phys.*, 9(1):349–352, 1922. 11

[26] Yun Li, Philipp Treutlein, Jakob Reichel, and Alice Sinatra. Spin squeezing in a bimodal condensate: spatial dynamics and particle losses. *Eur. Phys. J. B*, 68(3):365–381, 2009. 14

[27] M. Egorov, B. Opanchuk, P. Drummond, B. V. Hall, P. Hannaford, and A. I. Sidorov. Measurement of *s*-wave scattering lengths in a two-component Bose-Einstein condensate. *Phys. Rev. A*, 87:053614, May 2013. 14

[28] D. J. Wineland, J. J. Bollinger, W. M. Itano, and D. J. Heinzen. Squeezed atomic states and projection noise in spectroscopy. *Phys. Rev. A*, 50:67–88, Jul 1994. 15

[29] Luca Pezzé and Augusto Smerzi. Entanglement, nonlinear dynamics, and the Heisenberg limit. *Phys. Rev. Lett.*, 102:100401, Mar 2009. 17, 18

[30] Helmut Strobel, Wolfgang Muessel, Daniel Linnemann, Tilman Zibold, David B. Hume, Luca Pezzé, Augusto Smerzi, and Markus K. Oberthaler. Fisher information and entanglement of non-Gaussian spin states. *Science*, 345(6195):424–427, 2014. 18

[31] A. Sørensen, L.-M. Duan, J. I. Cirac, and P. Zoller. Many-particle entanglement with Bose-Einstein condensates. *Nature*, 409(6816):63–66, 01 2001. 18

[32] Anders S. Sørensen and Klaus Mølmer. Entanglement and extreme spin squeezing. *Phys. Rev. Lett.*, 86:4431–4434, May 2001. 18

[33] Philipp Hyllus, Luca Pezzé, Augusto Smerzi, and Géza Tóth. Entanglement and extreme spin squeezing for a fluctuating number of indistinguishable particles. *Phys. Rev. A*, 86:012337, Jul 2012. 18

[34] John Stewart Bell. On the Einstein Podolsky Rosen paradox. *Physics*, 1:195–200, 1964. 19

[35] J. Tura, R. Augusiak, A. B. Sainz, T. Vértesi, M. Lewenstein, and A. Acín. Detecting nonlocality in many-body quantum states. *Science*, 344(6189):1256–1258, 2014. 19

[36] Nicolas Gisin. Bell's inequality holds for all non-product states. *Phys. Lett. A*, 154(5):201 – 202, 1991. 20

[37] M. Paris and J. Řeháček, editors. *Quantum State Estimation*, volume 649 of *Lect. Notes Phys.* Springer, Berlin Heidelberg, 2004. 21, 56

[38] Z. Hradil, J. Řeháček, J. Fiurášek, and M. Ježek. *Maximum-Likelihood Methods in Quantum Mechanics*, chapter 3 of Ref. [37], pages 59–112. 22

[39] W. P. Schleich. *Quantum Optics in Phase Space*. Wiley-VCH, Berlin, 2001. 24

[40] G. S. Agarwal. Relation between atomic coherent-state representation, state multipoles, and generalized phase-space distributions. *Phys. Rev. A*, 24(6):2889–2896, 1981. 25, 26, 27

[41] J. P. Dowling, G. S. Agarwal, and W. P. Schleich. Wigner distribution of a general angular-momentum state: Applications to a collection of two-level atoms. *Phys. Rev. A*, 49(5):4101–4109, 1994. 25

[42] Matthias Christandl and Renato Renner. Reliable quantum state tomography. *Phys. Rev. Lett.*, 109:120403, Sep 2012. 27

[43] https://commons.wikimedia.org/wiki/File:Hammer_projection_SW.jpg licensed under CC BY-SA 3.0 (https://creativecommons.org/licenses/by-sa/3.0/deed.en). 29

[44] Thierry Giamarchi. *Quantum Physics in One Dimension*. International Series of Monographs on Physics. Oxford University Press, USA, 2004. 31

[45] Philipp Hans-Jürgen Hauke. *Quantum simulations with ultracold atoms: beyond standard optical lattices*. PhD thesis, Institut de Ciènces Fotòniques, Castelldefels, Spain, 2012. 31

[46] Philipp Hauke, Tommaso Roscilde, Valentin Murg, J. Ignacio Cirac, and Roman Schmied. Modified spin-wave theory with ordering vector optimization: frustrated bosons on the spatially anisotropic triangular lattice. *New J. Phys.*, 12(5):053036, May 2010. 31, 32

[47] Roman Schmied, Janus H. Wesenberg, and Dietrich Leibfried. Optimal surface-electrode trap lattices for quantum simulation with trapped ions. *Phys. Rev. Lett.*, 102:233002, Jun 2009. 31, 35, 51

[48] Christian Schneider, Diego Porras, and Tobias Schaetz. Experimental quantum simulations of many-body physics with trapped ions. *Rep. Prog. Phys.*, 75(2):024401, 2012. 32

[49] F. N. Krauth, J. Alonso, and J. P. Home. Optimal electrode geometries for 2-dimensional ion arrays with bi-layer ion traps. *J. Phys. B*, 48(1):015001, 2015. 32

[50] V. Y. F. Leung, A. Tauschinsky, N. J. van Druten, and R. J. C. Spreeuw. Microtrap arrays on magnetic film atom chips for quantum information science. *Quantum Inf. Process.*, 10:955–974, 2011. 32, 52

[51] V. Y. F. Leung, D. R. M. Pijn, H. Schlatter, L. Torralbo-Campo, A. L. La Rooij, G. B. Mulder, J. Naber, M. L. Soudijn, A. Tauschinsky, C. Abarbanel, B. Hadad, E. Golan, R. Folman, and R. J. C. Spreeuw. Magnetic-film atom chip with 10 μm period lattices of microtraps for quantum information science with Rydberg atoms. *Rev. Sci. Instr.*, 85(5), May 2014. 32, 46, 47, 52

[52] I. Herrera, Y. Wang, P. Michaux, D. Nissen, P. Surendran, S. Juodkazis, S. Whitlock, R. J. McLean, A. Sidorov, M. Albrecht, and P. Hannaford. Sub-micron period lattice structures of magnetic microtraps for ultracold atoms on an atom chip. *J. Phys. D*, 48(11):115002, 2015. 32

[53] Joseba Alonso, Florian M. Leupold, Ben C. Keitch, and Jonathan P. Home. Quantum control of the motional states of trapped ions through fast switching of trapping potentials. *New J. Phys.*, 15(2):023001, 2013. 32

[54] Arezoo Mokhberi and Stefan Willitsch. Sympathetic cooling of molecular ions in a surface-electrode ion trap. *Phys. Rev. A*, 90:023402, Aug 2014. 32

[55] Jakob Hammer, Johannes Hoffrogge, Stephan Heinrich, and Peter Hommelhoff. Phase-resolved electron guiding in optimized chip-based microwave potentials. *Phys. Rev. Applied*, 2:044015, Oct 2014. 32, 35

[56] Arezoo Mokhberi and Stefan Willitsch. Structural and energetic properties of molecular Coulomb crystals in a surface-electrode ion trap. *New J. Phys.*, 17(4):045008, 2015. 32

[57] Jakob Hammer, Sebastian Thomas, Philipp Weber, and Peter Hommelhoff. Microwave chip-based beam splitter for low-energy guided electrons. *Phys. Rev. Lett.*, 114:254801, Jun 2015. 32, 35

[58] Román Orús. A practical introduction to tensor networks: Matrix product states and projected entangled pair states. *Ann. Phys.*, 349:117–158, 2014. 32

[59] Alessio Celi, Tobias Grass, Andrew J. Ferris, Bikash Padhi, David Raventós, Juliette Simonet, Klaus Sengstock, and Maciej Lewenstein. Modified spin-wave theory and spin liquid behavior of cold bosons on an inhomogeneous triangular lattice. 2016, arXiv:1603.06561 [cond-mat.quant-gas]. 32

[60] Roman Schmied, Tommaso Roscilde, Valentin Murg, Diego Porras, and J. Ignacio Cirac. Quantum phases of trapped ions in an optical lattice. *New J. Phys.*, 10(4):045017, Apr 2008. 33

[61] Minoru Takahashi. Modified spin-wave theory of a square-lattice antiferromagnet. *Phys. Rev. B*, 40:2494–2501, Aug 1989. 33

[62] J. H. Xu and C. S. Ting. Modified spin-wave theory of low-dimensional quantum spiral magnets. *Phys. Rev. B*, 43:6177–6180, Mar 1991. 34

[63] Roman Schmied. Electrostatics of gapped and finite surface electrodes. *New J. Phys.*, 12(2):023038, Feb 2010. 34

[64] A. Van Oosterom and J. Strackee. The solid angle of a plane triangle. *IEEE Transac. Biomed. Eng.*, BME-30(2):125–126, Feb 1983. 35

[65] Mário H. Oliveira and José A. Miranda. Biot-Savart-like law in electrostatics. *Eur. J. Phys.*, 22(1):31, 2001. 35

[66] James D. Hanson and Steven P. Hirshman. Compact expressions for the Biot-Savart fields of a filamentary segment. *Phys. Plasmas*, 9:4410, 2002. 35

[67] D. L. Moehring, C. Highstrete, D. Stick, K. M. Fortier, R. Haltli, C. Tigges, and M. G. Blain. Design, fabrication and experimental demonstration of junction surface ion traps. *New J. Phys.*, 13(7):075018, 2011. 35

[68] Janus H. Wesenberg. Electrostatics of surface-electrode ion traps. *Phys. Rev. A*, 78:063410, Dec 2008. 36, 37

[69] Alexei Kitaev. Anyons in an exactly solved model and beyond. *Ann. Phys.*, 321(1):2 – 111, 2006. January Special Issue. 38, 39, 64

[70] David Deutsch. Quantum theory, the Church-Turing principle and the universal quantum computer. *Proc. R. Soc. Lond. A*, 400(1818):97–117, 1985. 44

[71] C. J. Ballance, T. P. Harty, N. M. Linke, M. A. Sepiol, and D. M. Lucas. Laser-driven quantum logic gates with precision beyond the fault-tolerant threshold. 2015, arXiv:1512.04600 [quant-ph]. 44

[72] J. P. Gaebler, T. R. Tan, Y. Lin, Y. Wan, R. Bowler, A. C. Keith, S. Glancy, K. Coakley, E. Knill, D. Leibfried, and D. J. Wineland. High-fidelity universal gate set for $^{9}Be^{+}$ ion qubits. 2016, arXiv:1604.00032 [quant-ph]. 44

[73] Tzvetan S. Metodi, Darshan D. Thaker, Andrew W. Cross, Frederic T. Chong, and Isaac L. Chuang. A quantum logic array microarchitecture: Scalable quantum data movement and computation. *International Symposium on Microarchitecture (MICRO-38)*, 2005. 44

[74] R. B. Blakestad, C. Ospelkaus, A. P. VanDevender, J. H. Wesenberg, M. J. Biercuk, D. Leibfried, and D. J. Wineland. Near-ground-state transport of trapped-ion qubits through a multidimensional array. *Phys. Rev. A*, 84:032314, Sep 2011. 44

[75] Janus H. Wesenberg. Ideal intersections for radio-frequency trap networks. *Phys. Rev. A*, 79:013416, Jan 2009. 46

[76] Vanessa Leung, Daniël Pijn, Hugo Schlatter, Lara Torralbo-Campo, Arthur La Rooij, Gijs Mulder, Julian Naber, Maarten Soudijn, Atreju Tauschinsky, and Robert Spreeuw. Experimental realization of novel lattice geometries of trapped atoms on a magnetic film atomchip for quantum simulation via Rydberg interactions. In *Research in Optical Sciences*. Optical Society of America, 2014, http://doi.org/10.1364/QIM.2014.QTh3A.2. 46, 47, 52

[77] Lao-tzu and Stephen Mitchell. *Tao Te Ching (chapter 17)*. Harper Perennial Modern Classics, New York, 2006. 51

My publications since 2010

During my stay at the Department of Physics of the University of Basel, I have contributed to the publication of the following works. All of these, with the exception of Refs. [6, 10], are published in reputable peer-reviewed scientific journals.

[1] Bell Correlations in a Bose-Einstein Condensate
Science 352(6284):441-444 (April 2016)
(see section 1.6 and page 67)
Characterizing many-body systems through the quantum correlations between their constituent particles is a major goal of quantum physics. Although entanglement is routinely observed in many systems, we report here the detection of stronger correlations – Bell correlations – between the spins of about 480 atoms in a Bose-Einstein condensate. We derive a Bell correlation witness from a many-particle Bell inequality involving only one- and two-body correlation functions. Our measurement on a spin-squeezed state exceeds the threshold for Bell correlations by 3.8 standard deviations. Our work shows that the strongest possible nonclassical correlations are experimentally accessible in many-body systems, and that they can be revealed by collective measurements.

[2] Arrays of individually controlled ions suitable for two-dimensional quantum simulations
Nature Communications 7:11839 (June 2016)
(see subsection 2.2.2 and page 89)
A precisely controlled quantum system may reveal a fundamental understanding of another, less accessible system of interest. A universal quantum computer is currently out of reach, but an analogue quantum simulator that makes relevant observables, interactions and states of a quantum model accessible could permit insight into complex dynamics. Several platforms have been suggested and proof-of-principle experiments have been conducted. Here, we operate two-dimensional arrays of three trapped ions in individually controlled harmonic wells forming equilateral triangles with side lengths 40 and 80 μm. In our approach, which is scalable to arbitrary two-dimensional lattices, we demonstrate

individual control of the electronic and motional degrees of freedom, preparation of a fiducial initial state with ion motion close to the ground state, as well as a tuning of couplings between ions within experimental sequences. Our work paves the way towards a quantum simulator of two-dimensional systems designed at will.

[3] Sideband Rabi spectroscopy of finite-temperature trapped Bose gases

Physical Review A 93:043624 (April 2016)

(see section 1.1 and page 99)

We use Rabi spectroscopy to explore the low-energy excitation spectrum of a finite-temperature Bose gas of Rubidium atoms across the phase transition to a Bose-Einstein condensate (BEC). To record this spectrum, we coherently drive the atomic population between two spin states. A small relative displacement of the spin-specific trapping potentials enables sideband transitions between different motional states. The intrinsic non-linearity of the motional spectrum, mainly originating from two-body interactions, makes it possible to resolve and address individual excitation lines. Together with sensitive atom-counting, this constitutes a feasible technique to count single excited atoms of a BEC and to determine the temperature of nearly pure condensates. As an example, we show that for a nearly pure BEC of $N = 800$ atoms the first excited state has a population of less than 5 atoms, corresponding to an upper bound on the temperature of 30 nK.

[4] Quantum State Tomography of a Single Qubit: Comparison of Methods

Journal of Modern Optics 63(18):1744 (January 2016)

(see section 1.7 and page 105)

The tomographic reconstruction of the state of a quantum-mechanical system is an essential component in the development of quantum technologies. We present an overview of different tomographic methods for determining the quantum-mechanical density matrix of a single qubit: (scaled) direct inversion, maximum likelihood estimation (MLE), minimum Fisher information distance, and Bayesian mean estimation (BME). We discuss the different prior densities in the space of density matrices, on which both MLE and BME depend, as well as ways of including experimental errors and of estimating tomography errors. As a measure of the accuracy of these methods we average the trace distance between a given density matrix and the tomographic density matrices it can give rise to through experimental measurements. We find that the BME provides the most accurate estimate of the density matrix, and suggest using either the pure-state prior, if the system is known to be in a rather pure state, or the Bures prior if any state is possible. The MLE is found to be slightly less accurate. We comment on the extrapolation of these

results to larger systems.

[5] Tighter quantum uncertainty relations following from a general probabilistic bound
Physical Review A 92:012102 (July 2015)
(see section 1.2 and page 121)
Uncertainty relations (URs) such as the Heisenberg-Robertson or the time-energy UR are often considered to be hallmarks of quantum theory. Here, a simple derivation of these URs is presented based on a single classical inequality from estimation theory, a Cramér-Rao-like bound. The Heisenberg-Robertson UR is then obtained by using the Born rule and the Schrödinger equation. This allows a clear separation of the probabilistic nature of quantum mechanics from the Hilbert space structure and the dynamical law. It also simplifies the interpretation of the bound. In addition, the Heisenberg-Robertson UR is tightened for mixed states by replacing one variance by the quantum Fisher information. Thermal states of Hamiltonians with evenly gapped energy levels are shown to saturate the tighter bound for natural choices of the operators. This example is further extended to Gaussian states of a harmonic oscillator. For many-qubit systems, we illustrate the interplay between entanglement and the structure of the operators that saturate the UR with spin-squeezed states and Dicke states.

[6] Lecture script: Introduction to Computational Quantum Mechanics
arXiv:1403.7050 [quant-ph] (since 2014)
(see chapter 3 and page 127)
This document is the lecture script of a one-semester course taught at the University of Basel in the Fall semesters of 2012 and 2013 and in the Spring semester of 2015. It is aimed at advanced students of physics who are familiar with the concepts and notations of quantum mechanics. Quantum mechanics lectures can often be separated into two classes. In the first class you get to know Schrödinger's equation and find the form and dynamics of simple physical systems (square well, harmonic oscillator, hydrogen atom); most calculations are analytic and inspired by calculations originally done in the 1920s and 1930s. In the second class you learn about large systems such as molecular structures, crystalline solids, or lattice models; these calculations are usually so complicated that it is difficult for the student to understand them in all detail. This lecture tries to bridge the gap between simple analytic calculations and complicated large-scale computations. We will revisit most of the problems encountered in introductory quantum mechanics, focusing on computer implementations for finding analytical as well as numerical solutions and their visualization. Most of these calculations are too complicated to be done by hand. Even relatively simple problems, such as

two interacting particles in a one-dimensional trap, do not have analytic solutions and require the use of computers for their solution and visualization. More complex problems scale exponentially with the number of degrees of freedom, and make the use of large computer simulations unavoidable. The course is taught using the Mathematica programming language; however, the concepts presented are readily translated to any other programming language.

[7] Quantum Metrology with a Scanning Probe Atom Interferometer

Physical Review Letters 111:143001 (October 2013)

(see section 1.4 and page 135)

We use a small Bose-Einstein condensate on an atom chip as an interferometric scanning probe to map out a microwave field near the chip surface with a few micrometers resolution. With the use of entanglement between the atoms, our interferometer overcomes the standard quantum limit of interferometry by 4 dB and maintains enhanced performance for interrogation times up to 10 ms. This corresponds to a microwave magnetic field sensitivity of 77 $\mathrm{pT}/\sqrt{\mathrm{Hz}}$ in a probe volume of 20 $\mu\mathrm{m}^3$. Quantum metrology with entangled atoms is useful in measurements with high spatial resolution, since the atom number in the probe volume is limited by collisional loss. High-resolution measurements of microwave near fields, as demonstrated here, are important for the development of integrated microwave circuits for quantum information processing and applications in communication technology.

[8] Quantum simulation of the hexagonal Kitaev model with trapped ions

New Journal of Physics 13(11):115001 (November 2011)

(see subsection 2.2.1 and page 141)

We present a detailed study of quantum simulations of coupled spin systems in surface-electrode (SE) ion-trap arrays, and illustrate our findings with a proposed implementation of the hexagonal Kitaev model [69]. The effective (pseudo)spin interactions making up such quantum simulators are found to be proportional to the dipole–dipole interaction between the trapped ions, and are mediated by motion that can be driven by state-dependent forces. The precise forms of the trapping potentials and the interactions are derived in the presence of an SE and a cover electrode. These results are the starting point to derive an optimized SE geometry for trapping ions in the desired honeycomb lattice of KitaevÕs model, where we design the dipole–dipole interactions in a way that allows for coupling all three bond types of the model simultaneously, without the need for time discretization. Finally, we propose a simple wire structure that can be incorporated into a microfabricated chip to generate localized state-dependent forces which drive the couplings prescribed by

this particular model; such a wire structure should be adaptable to many other situations.

[9] Modified spin-wave theory with ordering vector optimization II: spatially anisotropic triangular lattice and $J_1J_2J_3$ model with Heisenberg interactions

New Journal of Physics 13(7):075017 (July 2011)

(see section 2.1 and page 165)

We study the ground-state phases of the quantum antiferromagnet on the spatially anisotropic triangular lattice (SATL) and on the square lattice with up to next-next-nearest-neighbor coupling (the $J_1J_2J_3$ model), making use of Takahashi's modified spin-wave (MSW) theory supplemented by ordering vector optimization. We compare the MSW results with exact diagonalization and projected-entangled-pair-states calculations, demonstrating their qualitative and quantitative reliability. We find that the MSW theory correctly accounts for strong quantum effects on the ordering vector of the magnetic phases of the models under investigation: in particular, collinear magnetic order is promoted at the expense of non-collinear (spiral) order, and several spiral states that are stable at the classical level disappear from the quantum phase diagram. Moreover, collinear states and non-collinear ones are never connected continuously, but they are separated by parameter regions in which the MSW theory breaks down, signaling the possible appearance of a non-magnetic ground state. In the case of the SATL, a large breakdown region appears also for weak couplings between the chains composing the lattice, suggesting the possible occurrence of a large non-magnetic region continuously connected with the spin-liquid state of the uncoupled chains. This shows that the MSW theory is—despite its apparent simplicity—a versatile tool for finding candidate regions in the case of spin-liquid phases, which are among prime targets for relevant quantum simulations.

[10] SurfacePattern: a Mathematica package for surface atom and ion traps

https://atom.physik.unibas.ch/people/romanschmied/code/SurfacePattern.php (since July 2011)

(see section 2.2 and page 195)

The Mathematica package *SurfacePattern* is a collection of algorithms for calculating electric and magnetic fields above planar structures, both finite and periodic-infinite. It contains functions to create patterns in 2D from polygons and disks representing electrodes, permanently magnetized regions, or regions delimited by edge wires. From these, the potentials throughout space and their spatial derivatives are calculated. SurfacePattern also contains fast algorithms to calculate optimal 2D

patterns that generate desired fields specified by spatially localized constraints, *e.g.* specific spatial arrangements of ion traps or Ioffe–Pritchard atom traps. This package is freely available through the terms of the GNU Public License (Version 3).

[11] Tomographic reconstruction of the Wigner function on the Bloch sphere

New Journal of Physics 13(6):065019 (June 2011)

(see section 1.7 and page 199)

We present a filtered backprojection algorithm for reconstructing the Wigner function of a system of large angular momentum j from Stern–Gerlach-type measurements. Our method is advantageous over the full determination of the density matrix in that it is insensitive to experimental fluctuations in j, and allows for a natural elimination of high-frequency noise in the Wigner function by taking into account the experimental uncertainties in the determination of j, its projection m and the quantization axis orientation. No data binning and no arbitrary smoothing parameters are necessary in this reconstruction. Using recently published data [23], we reconstruct the Wigner function of a spin-squeezed state of a Bose–Einstein condensate of about 1250 atoms, demonstrating that measurements along quantization axes lying in a single plane are sufficient for performing this tomographic reconstruction. Our method does not guarantee positivity of the reconstructed density matrix in the presence of experimental noise, which is a general limitation of backprojection algorithms.

[12] Optimized magnetic lattices for ultracold atomic ensembles

New Journal of Physics 12(10):103029 (October 2010)

(see subsection 2.2.4 and page 217)

We introduce a general method for designing tailored lattices of magnetic microtraps for ultracold atoms on the basis of patterned permanently magnetized films. A fast numerical algorithm is used to automatically generate patterns that provide optimal atom confinement while respecting desired lattice symmetries and trap parameters. The algorithm can produce finite and infinite lattices of any plane symmetry; we focus specifically on square and triangular lattices, which are of interest for future experiments. Typical trap parameters, as well as the impact of realistic imperfections such as finite lithographic resolution and magnetic inhomogeneity, are discussed. The designer lattices presented open new avenues for quantum simulation and quantum information processing with ultracold atoms on atom chips.